AD-A263 514

NAVAL POSTGRADUATE SCHOOL
Monterey, California

THESIS

PRELIMINARY DEVELOPMENT
OF A VTOL UNMANNED AIR VEHICLE
FOR THE CLOSE-RANGE MISSION

by

Gregory A. Kress

September, 1992

Thesis Advisor: Richard M. Howard

93-09292

Security Classification of this page

REPORT DOCUMENTATION PAGE

1a Report Security Classification Unclassified		1b Restrictive Markings			
2a Security Classification Authority		3 Distribution Availability of Report			
2b Declassification/Downgrading Schedule		Approved for public release; distribution is unlimited.			
4 Performing Organization Report Number(s)		5 Monitoring Organization Report Number(s)			
6a Name of Performing Organization Naval Postgraduate School	6b Office Symbol (If Applicable) 55	7a Name of Monitoring Organization Naval Postgraduate School			
6c Address (city, state, and ZIP code) Monterey, CA 93943-5000		7b Address (city, state, and ZIP code) Monterey, CA 93943-5000			
8a Name of Funding/Sponsoring Organization	8b Office Symbol (If Applicable)	9 Procurement Instrument Identification Number			
8c Address (city, state, and ZIP code)		10 Source of Funding Numbers			
		Program Element Number	Project No	Task No	Work Unit Accession No

11 Title (Include Security Classification)
(Unclassified) Preliminary Development of a VTOL Unmanned Air Vehicle for the Close-Range mission.

12 Personal Author(s) Kress, Gregory A

13a Type of Report Master's Thesis	13b Time Covered From To	14 Date of Report (year, month,day) 1992 September 29	15 Page Count 88

16 Supplementary Notation The views expressed in this thesis are those of the author and do not reflect the official policy or position of the Department of Defense or the U.S. Government.

17 Cosati Codes			18 Subject Terms (continue on reverse if necessary and identify by block number)
Field	Group	Subgroup	Unmanned Air Vehicle, UAV, Tilting Ducted Fan (TDF), Tailsitter, Aquila, AROD, Thrust stand, Torque stand, composite

19 Abstract (continue on reverse if necessary and identify by block number)

The preliminary development of a full-scale Vertical Takeoff and Landing (VTOL) Unmanned Air Vehicle (UAV) for the Close-Range mission was completed at the Naval Postgraduate School (NPS). The vehicle was based on half-scale ducted-fan investigations performed at the UAV Flight Research Lab. The resulting design is a fixed-duct, tail-sitter UAV with a canard-configured horizontal stabilizer. Major airframe components are used from previous UAVs and include the wings from a U. S. Army Aquila and the ducted fan from the U.S. Marine Corps AROD. Accomplishments include: 1.) the design and fabrication of a carry-through spar and 2.) the design and construction of an engine test stand. The through spar was designed using finite element analysis and constructed from composite materials. The purpose of the test stand is to measure torque, horsepower, and thrust of an entire ducted fan or an individual engine. Completion of this thesis will pave the way for future NPS research into the growing interest in VTOL UAV technology.

20 Distribution/Availability of Abstract [X] unclassified/unlimited [ ] same as report [ ] DTIC users	21 Abstract Security Classification Unclassified	
22a Name of Responsible Individual Professor Richard Howard	22b Telephone (Include Area code) (408) 646-2870	22c Office Symbol AA/HO

DD FORM 1473, 84 MAR   83 APR edition may be used until exhausted   security classification of this page
All other editions are obsolete   Unclassified

**Preliminary Development
of a VTOL Unmanned Air Vehicle
for the Close-Range Mission**

by

**Gregory A. Kress
Lieutenant, United States Navy
B.S., Southern Illinois University, 1984**

Submitted in partial fulfillment of
the requirements for the degree of

**MASTER OF SCIENCE IN AERONAUTICAL
ENGINEERING**

from the

**NAVAL POSTGRADUATE SCHOOL
September, 1992**

Author: _____
Gregory A. Kress
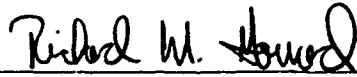
Approved by: _____
Richard M. Howard, Thesis Advisor
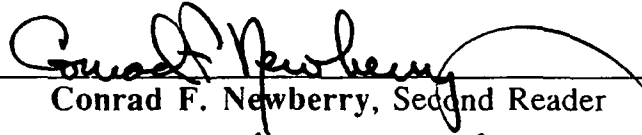
_____
Conrad F. Newberry, Second Reader

_____
Daniel J. Collins, Chairman
Department of Aeronautics and Astronautics

ABSTRACT

The preliminary development of a full-scale Vertical Takeoff and Landing (VTOL) Unmanned Air Vehicle (UAV) for the Close-Range mission was completed at the Naval Postgraduate School (NPS). The vehicle was based on half-scale ducted-fan investigations performed at the UAV Flight Research Lab. The resulting design is a fixed-duct, tail-sitter UAV with a canard-configured horizontal stabilizer. Major airframe components are used from previous UAVs and include the wings from a U. S. Army Aquila and the ducted fan from the U.S. Marine Corps AROD. Accomplishments include: 1.) the design and fabrication of a carry-through spar and 2.) the design and construction of an engine test stand. The carry-through spar was designed using finite element analysis and constructed from composite materials. The purpose of the test stand is to measure torque, horsepower, and thrust of an entire ducted fan or an individual engine. Completion of this thesis will pave the way for future NPS research into the growing interest in VTOL UAV technology.

Accesion For		
NTIS CRA&I	☑	
DTIC TAB	☐	
Unannounced	☐	
Justification		
By		
Distribution /		
Availability Codes		
Dist	Avail and / or Special	
A-1		

iii

TABLE OF CONTENTS

TABLE OF SYMBOLS

E_1 .... Young's modulus in the, 1, primary direction.

E_2 .... Young's modulus in the, 2, primary direction.

υ_{12} .... Longitudinal Poisson's ratio.

G_{12} .... Longitudinal shear modulus.

N_x .... Normal force component in the x-direction.

N_y .... Normal force component in the y-direction.

N_{xy} .... Shear force component, x, in the y-direction.

M_x .... Moment component in the x-direction.

M_y .... Moment component in the y-direction.

M_{xy} .... Moment x-component in the y-direction.

A_{ij} .... Extensional matrix component.

B_{ij} .... Extension/bending coupling matrix component.

D_{ij} .... Bending matrix component.

ε_x .... X-component of normal strain.

ε_y .... Y-component of normal strain.

ε_{xy} .... XY shear strain.

κ_x .... X-component of curvature.

κ_y .... Y-component of curvature.

κ_{xy} .... X-component of curvature in the y-direction.

β .... Ply angle.

$\overline{Q}_{ij}$ .... Transformed reduced stiffness matrix component.

Q_{ij} .... Reduced stiffness matrix component.

h_j .... Laminate thickness from the midplane.

WS .... Wing station.

MAC .... Mean aerodynamic chord.

CG .... Center of gravity.

M .... Mach number.

Fv .... Fiber volume.

g .... Gravity.

t .... Thickness.

Hp .... Horse power.

RPM................................ Rotations per minute.

RHO................................ Laminate density .

FT................................ Ultimate tensile strength.

FC................................ Ultimate conpressive strength .

F................................ Ultimate shear strength (appendix C).

FAW................................ Fiber areal weight .

RC................................ Resin content.

VV................................ Void volume.

TPLY................................ Ply thickness .

LYR................................ Laminate layer.

MAT................................ Laminate material.

ANGLE................................ Ply angle.

ID................................ Ply identification number.

τ................................ Normal shear.

σ................................ Normal stress.

k................................ Shear constant.

V................................ Shear.

A................................ Area (appendix D.).

Q................................ First moment.

I................................ Moment of itertia.

t................................ Thickness .

M................................ Moment .

F................................ Force .

c................................ Radius .

T................................ Torque .

J................................ Polar moment of inerial .

α................................ Area bound by beam centerline .

P................................ Load .

F................................ Wing station.

ACKNOWLEDGMENTS

I. INTRODUCTION

A. THE NEED FOR UNMANNED AIR VEHICLES

The Unmanned Air Vehicle (UAV) began maturity in a warfare role when in 1960 an aerial camera was mounted to the airframe of a Ryan Q-2C Firebee target drone to adapted the vehicle for photographic surveillance missions [Ref. 1]. At that moment United States military strategists realized that a UAV could be placed in an tactical environment to perform high-risk reconnaissance missions without endangering more expensive aircraft and aircrew. Over the past 30 years UAVs have been adapted into a multitude of roles including surveillance, weather monitoring, communications relay, reconnaissance, over-the-horizon targeting, and damage assessment. To perform these missions the field of UAVs has been developed to cover the entire spectrum from high-speed jet vehicles to low-speed hovering configurations.

A need exists in the Close-Range role to have a vehicle that exhibits Vertical Takeoff and Landing (VTOL) capabilities and is also able to rapidly transit to an onstation position. The UAV Joint Project Office (JPO) in Washington D.C. has contracted technology demonstrators for a vehicle with a takeoff weight of under 200 lbs., a 50 lb. payload, and a maximum speed of 150 kts. The aircraft must be able to takeoff and land within an area 30m x 60m with an obstacle clearance of 15 meters. Many variations of helicopter-type UAVs have been developed but are limited to horizontal flight speeds of approximately 70 knots. [Ref. 2, p.50]

1

B. THE NATURE OF UAV RESEARCH AT NPS

The role of the Unmanned Air Vehicle Flight Research Lab (UAV FRL) at the Naval Postgraduate School is to lead and support the advances in UAV research and technology. The UAV FRL is uniquely able to fill this role by providing a wide base of aeronautical knowledge from both the fixed-wing and helicopter communities of all branches of the military. Over the recent years the UAV FRL has obtained an Aquila airframe and several complete Airborne Remotely Operated Device (AROD) vehicles [Ref. 3, p.73] from the Naval Command and Control and Ocean Surveillance Center RTD & E Division Detachment to serve as a basis for continuing its research.

From a design standpoint each of these UAVs is very unique. The Aquila possessed a strong, light-weight airframe made from advanced composite materials; however, it required additional equipment for a catapult launch and net recovery. A powerful ducted fan and stability augmentation system enabled the AROD to achieve its VTOL capabilities and to sustain hovering flight. Reliance on powered lift allowed the AROD to meet its requirement as a stationary camera platform but made it unable to achieve transit airspeeds of greater than 30 knots. Working with these two concepts, the UAV FRL is developing a vehicle to meet the JPO goals by combining the benefits and advances from each of these UAV platforms while minimizing the disadvantages that each one possessed. This thesis initiated the research on a full-scale proof-of-concept vehicle to meet this goal. The research involves the development of a new VTOL configuration, the design of a test stand for ground run-up of the powerplant, and the design, testing and fabrication of a new wing center structure. This full-scale UAV is based on the past research of Ellwood [Ref. 4],

Blanchette [Ref. 5], and Brynestad [Ref. 6]. They developed and tested a half-scale model to identify problems associated with a vehicle designed to achieve both vertical and horizontal flight. The half-scale design encountered difficulties in static thrust available, in excess weight, and in the need for a complex tilting-duct mechanism. These deficiencies are corrected in the full-scale vehicle by using the high-strength, lightweight airframe components from the Aquila and AROD airframes and the superior duct design of the AROD to provide efficient static thrust. The full-scale model has a new wing center structure designed by computer finite element analysis methods and constructed of advanced composite materials.

II. BACKGROUND

A. AQUILA

Development of the U. S. Army Aquila (XMQM-105) began as a program to provide a UAV technology demonstrator. The air vehicle was developed under Lockheed's proposal, Remotely Piloted Vehicle System Technology Demonstrator Program (RPV-STD) for the U. S. Army, LMSC-D056091, 30 August 1974. The Aquila was developed for a principal mission of surveillance, target acquisition, fire adjustment, and damage assessment in support of Army artillery and ground forces. The vehicle is configured as a flying-wing aircraft with a wing span of 12 feet, 3 inches. The general arrangement of the Aquila is shown in Figure 2.1. [Ref. 6]
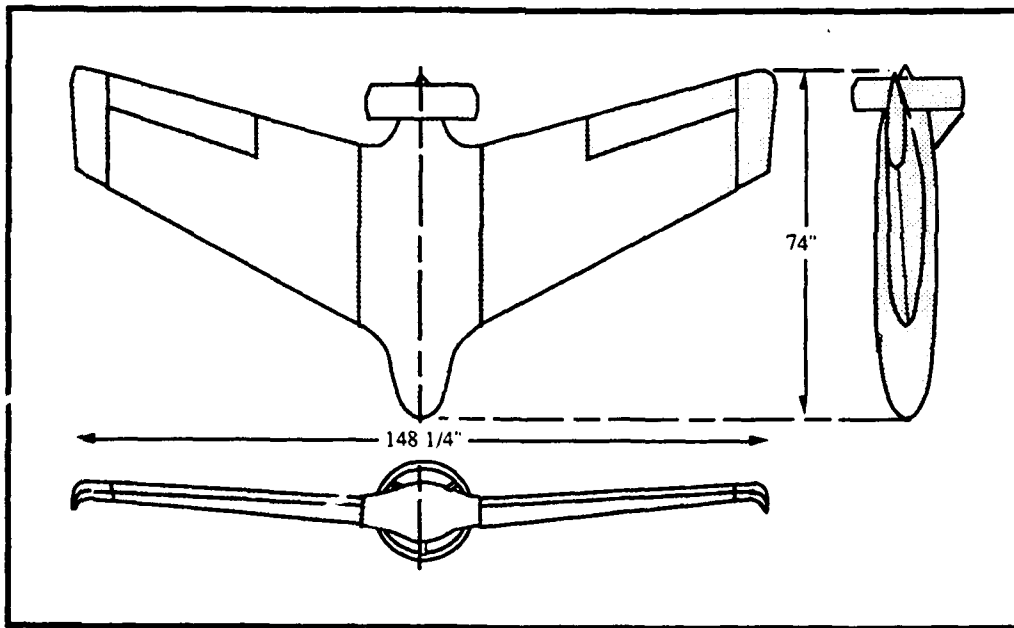

Figure 2.1. Aquila three view diagram.

Before final production ended, the Aquila had seen many modifications to its structural and aerodynamic design. The Aquila airframe obtained by the Naval Postgraduate School is from the manufacture period between December 1974 to December 1977. Table 2.1 lists the characteristics of the Aquila configuration [Ref. 7, p.39].

Table 2.1. AQUILA CHARACTERISTICS.

Wing area (projected)	31.4 feet^2
Wing span (overall)	12.35 feet
Wing area (reference)	30.3 feet^2
Wing span (reference)	11.5 feet
Root chord (WS 13)	36.73 inches
Tip chord (WS 69)	23 inches
Mean Aerodynamic Chord (MAC)	32.26 inches
Aspect ratio (overall)	4.86
Taper ratio	0.58
Sweep, Leading edge	28 degrees
Sweep, .25 chord	25.2 degrees
Dihedral, Trailing edge	4 degrees
Incidence (WS 13)	+3 degrees
Incidence (WS 69)	0 degrees
Airfoil section	modified NACA 23015
Forward CG location	20% MAC
Aft CG location	22% MAC
Maximum gross weight	160 lbs (at sea level)
Wing loading	4 lb/ft^2
Power loading	12 lb/hp

The significant features of the vehicle are:

- Swept wing.
- Shrouded pusher propeller.
- Removable wings for storage.
- Lightweight Kevlar® construction.
- Pneumatic rail launch.
- Vertical barrier net recovery.

The airframe is constructed of advanced composite materials. Structural strength and stiffness are provided through the use of composite sandwich construction. This construction technique reduces the need and extra weight associated with the conventional method of rib, bulkhead, and stringer structural design. The fuselage is designed of varying elliptical cross section which is faired very smoothly into the 28° swept wing to provide a very low radar cross section. Power is provided with an aft-mounted ducted propeller. The propeller shroud provides increased safety to operating personnel during ground launch procedures and protection to the propeller during net capture, while also providing directional and longitudinal stability. Flight control was accomplished through movable elevons on the wing. A major downfall was that the vehicle required a large crew of ground personal and a considerable inventory of equipment for launch, control, and recovery.

B. AROD

The AROD was designed by the Sandia Research Laboratory in Albuquerque, New Mexico. This vehicle was designed for a reconnaissance and surveillance mission for the United States Marine Corps. It differed significantly from the Aquila in that it was capable of vertical takeoff and landing. The AROD possessed no flying surfaces and relied solely on powered lift. Control

6

was obtained through four fixed anti-torque vanes and four moveable control vanes, all positioned in the propeller wash of the duct. Its main features were:

- VTOL flight capabilities.
- Lightweight graphite construction.
- Compact size.
- Minimal crew and support equipment.
- Advanced digital stability augmentation system.

The AROD suffered from inefficiencies associated with hovering flight for a small-diameter powered-lift platform. Since most of the engine output was used to maintain powered lift [FIG. 2.2], there was little excess thrust available to increase the forward speed. A benefit associated with the AROD was the greater static performance provided by the efficient design of the ducted fan. The addition of a shroud around the AROD's three-bladed propeller significantly reduced the contraction of the slipstream associated with normal propellers. This result increased the mass flow through the fan and produced more static thrust than a conventional propeller configuration [Ref. 8, p.1]. Table 2.2 lists the measurements taken from the AROD.

The improvements in thrust for a ducted fan are directly related to its geometrical design. Based on the values in Table 2.1, the data from Reference 8 predict the following benefits in thrust available with the AROD's design.

1. A 50% increase in static thrust at a tip speed of 700 fpm over a conventional propeller and 66% increase at 800 fpm.
2. Inlet area ratio of 1.219 is optimal below M=0.3.
3. Exit area ratio of 1.115 is most beneficial above M=0.1.
4. The shroud length of 14 inches is optimal below M=0.3.

7

5. The propeller position at 25% chord is the most efficient location for all airspeeds.

6. The three-bladed propeller provides greater thrust over an increased number of blades below M=0.1.

7. The blade tip clearance of 0.00258 (clearance/diameter) optimizes the thrust below M=0.2.

Table 2.2. AROD CHARACTERISTICS.

Inlet diameter	29.25 inches
Propeller diameter, D	24 inches
Exit diameter	26.75 inches
Inlet area ratio	1.219
Exit area ratio	1.115
Exterior contour	tapered rear
Propeller location, %c	25%
Number of blades	3
Tip clearance	0.031 ± 0.005 inches
Tip clearance (clearance/dia.)	.00258
Engine speed, maximum	8000 rpm
Engine speed, nominal	7000 rpm
Tip speed, maximum	838 fpm
Tip speed, nominal	733 fpm
Power loading, $\frac{BHP\,(\rho_o/\rho)}{D^2}$	7.25 Hp/ft^2
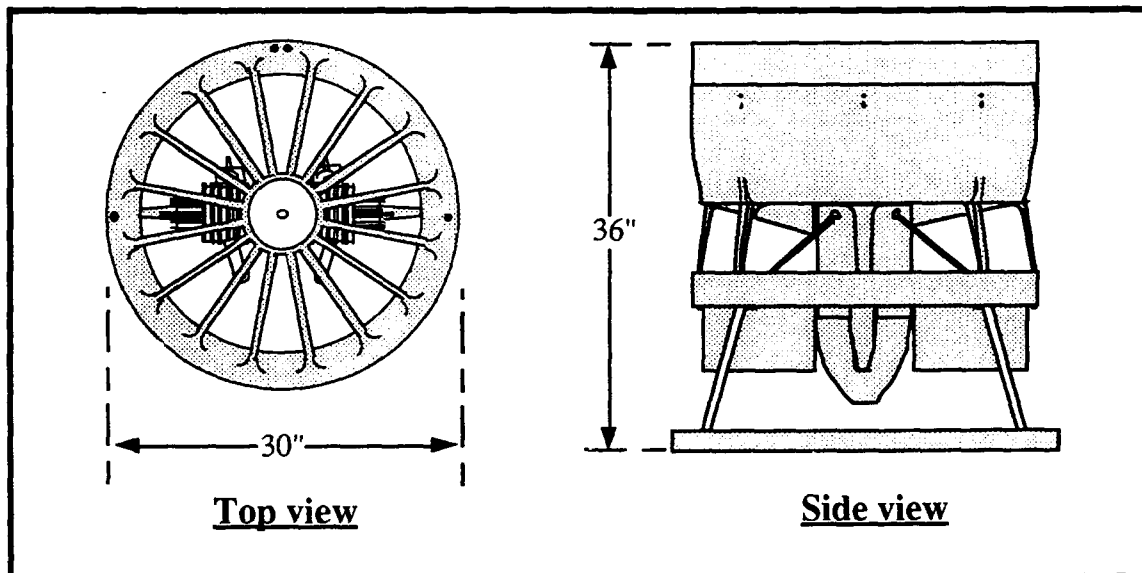
Figure 2.2. AROD diagram.

C. ARCHYTAS TDF

Initial work on the proof-of-concept VTOL UAV evolved from the theses of Blanchette, Ellwood, and Brynestad. This design was named the Archytas after the 500 BC Greek scientist and mathematician credited with the design and construction of a mechanical flying bird. The Archytas was configured as a fixed-wing vehicle constructed from composite materials. It incorporated a fuselage and wings that were modeled after a half-scale Aquila. The fuselage had the aft center portion removed to accommodate a tilting ducted fan (TDF) located at the center of gravity. [Ref. 4]

The powerplant modeled the AROD by housing an engine-driven fan in a circular duct. The fan was manually rotated to direct the thrust downward for vertical flight with control given by vanes mounted in the ducted-fan slipstream. For horizontal flight the fan could be positioned to redirect the thrust aft. Sufficient thrust was available for horizontal flight; however, vertical flight was

9

never achieved. The shroud for the Archytas was designed with an exit area ratio of 1.0. Even though this value will prevent contraction of the propeller slipstream, it will only increase the static thrust by 26% over a conventional propeller [Ref. 8, p.1]. The duct alone was successfully hovered in tethered flight with the assistance of a rate gyro [Ref. 6].

Three versions of the Archytas were proposed: a tailless model, a short-coupled tail design, and a long boom tail configuration [Ref. 4]. The long boom Archytas vehicle is shown in Figure 2.3. For purpose of discussion here this version will be referred to as the Archytas TDF. Lessons learned from the Archytas TDF research were:

1. Optimization of ducted-fan design is essential to gain the necessary static thrust required for vertical flight.
2. Incorporation of a tilting mechanism to allow transition between vertical and horizontal flight presents a major difficulty.
3. The structural design of the airframe must be optimized to keep the total airframe weight at an absolute minimum.

The design of the Archytas TDF was strictly intended as a proof-of-concept vehicle to examine the flight capabilities in the horizontal and vertical modes. The half-scale size did not provide sufficient internal space to house the mechanisms necessary for inflight transition, nor was it designed to do so. The half-scale platform was conceived to fly in both horizontal and vertical modes, but not to perform the transition maneuver. Further development on propeller design for increased thrust for the half-scale UAV continues.
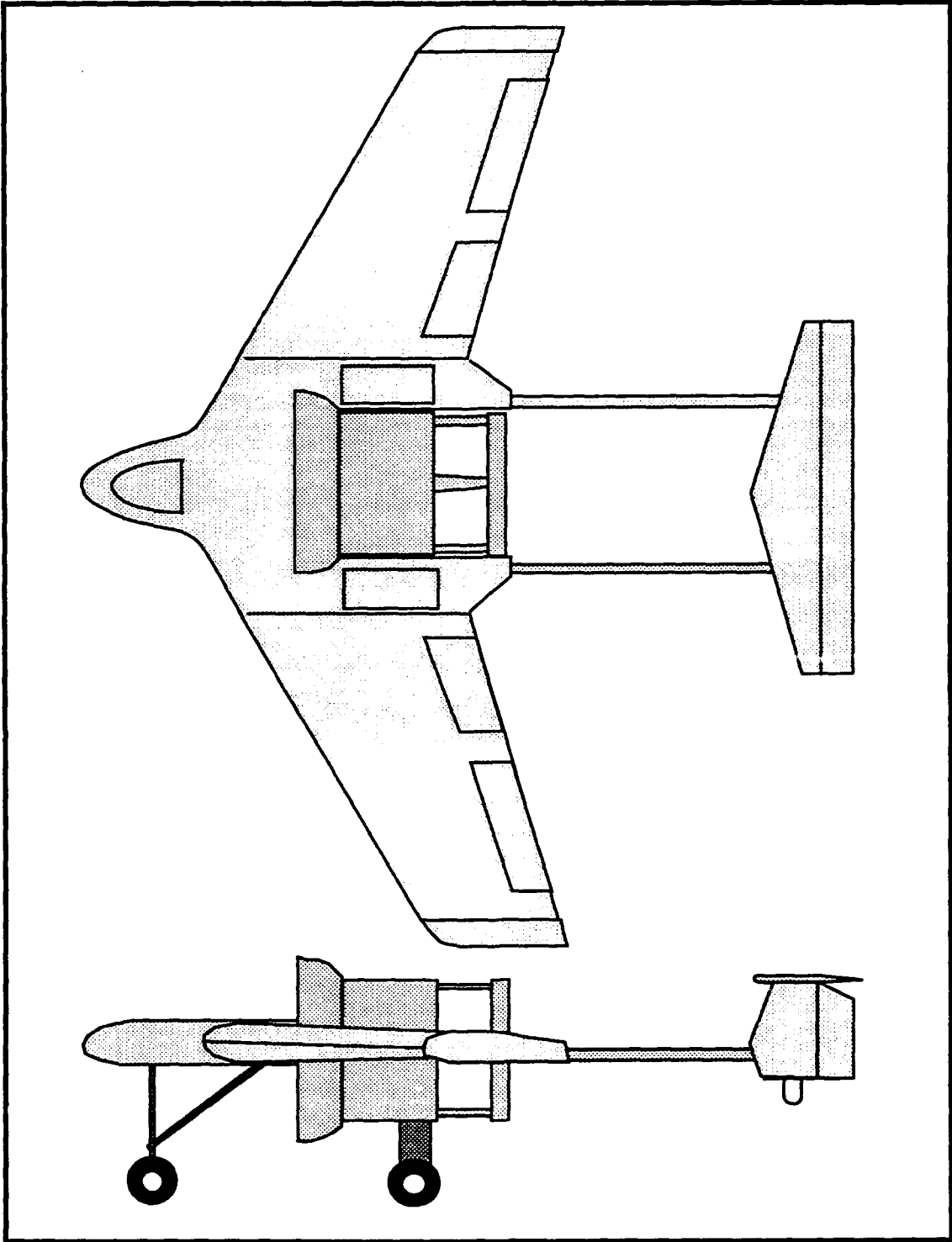
Figure 2.3. Archytas TDF.

III. ARCHYTAS TS CONFIGURATION

A. CURRENT RESEARCH

This thesis proceeded with the development of the full-scale proof-of-concept VTOL UAV. The redesigned Archytas allowed direct assembly of the Aquila wings to the AROD duct. The research involved the re-evaluation of the Archytas TDF configuration, the construction of a larger and more efficient engine test stand, and the design and fabrication of the complex carry-through spar required to incorporate the wings and the ducted fan into a single airframe. The final Archytas configuration involved many modifications from the initial Archytas TDF design. The most significant change included the use of a fixed duct rather than a tilting duct. This use enabled a simpler fuselage structure and withdrew the requirement for a complex tilting mechanism for the duct. The new design incorporated a configuration referred to as a tail-sitter (TS). From this concept came the new name Archytas TS. A horizontal stabilizer was added to the design to provide longitudinal stability in forward flight.

B. ARCHYTAS TS STRUCTURAL COMPONENTS

Configuration of the Archytas TS considered four primary factors. 1.) Foremost was the desire that the airframe components from the AROD and the Aquila be joined with minimal addition of structural components. This would decrease the complexity and lessen the addition of weight. 2.) The new vehicle would avoid any modifications to the AROD or Aquila components that would reduce their performance or weaken their structural integrity. 3.) The airframe design would eliminate any fuselage structure that could interfere with the

12

airflow through the duct. 4.) The landing gear would not add any additional weight but still provide stability while the UAV was on the ground. These considerations resulted in the design shown in Figure 3.1.

1. Archytas TS wings

The wings for the Archytas TS were taken directly from the Aquila with no modification to their structure. The airfoil is a modified NACA 23015. Coordinates for the airfoil are listed in Appendix A. Aerodynamic loads on the wings are supported by two spars positioned at the 25% and 70% chord location. The primary material used in the wing construction is a Kevlar/epoxy composite. Kevlar® is a high strength, light-weight material with the fiber properties listed in Appendix A. [Ref. 7]

The airfoil shape was maintained without ribs by the use of stiffened wing skins. These skins were built using a molded sandwich construction with a 0.25-inch Nomex® honeycomb core. The wing skins were then bonded to the forward and aft spars to form the leading edge d-cell and center torque box. The trailing edge of the wing was filled with an epoxy/microsphere slurry to reinforce the joint of the upper and lower wing skins. Elevons were located at the outboard portion of each wing panel. Construction of the elevons was similar to that of the main wings except that the elevons use a solid honeycomb core. The elevons pivot on hinges mounted to the aft spar. Actuation of the elevons is provided by direct linkage to electronic servos. The laminate properties for wing materials are listed in Appendix A. [Ref. 7]

2. Forward fuselage and canard

An additional horizontal stabilizer was incorporated in the design to provide increased longitudinal stability and control while flying in the horizontal
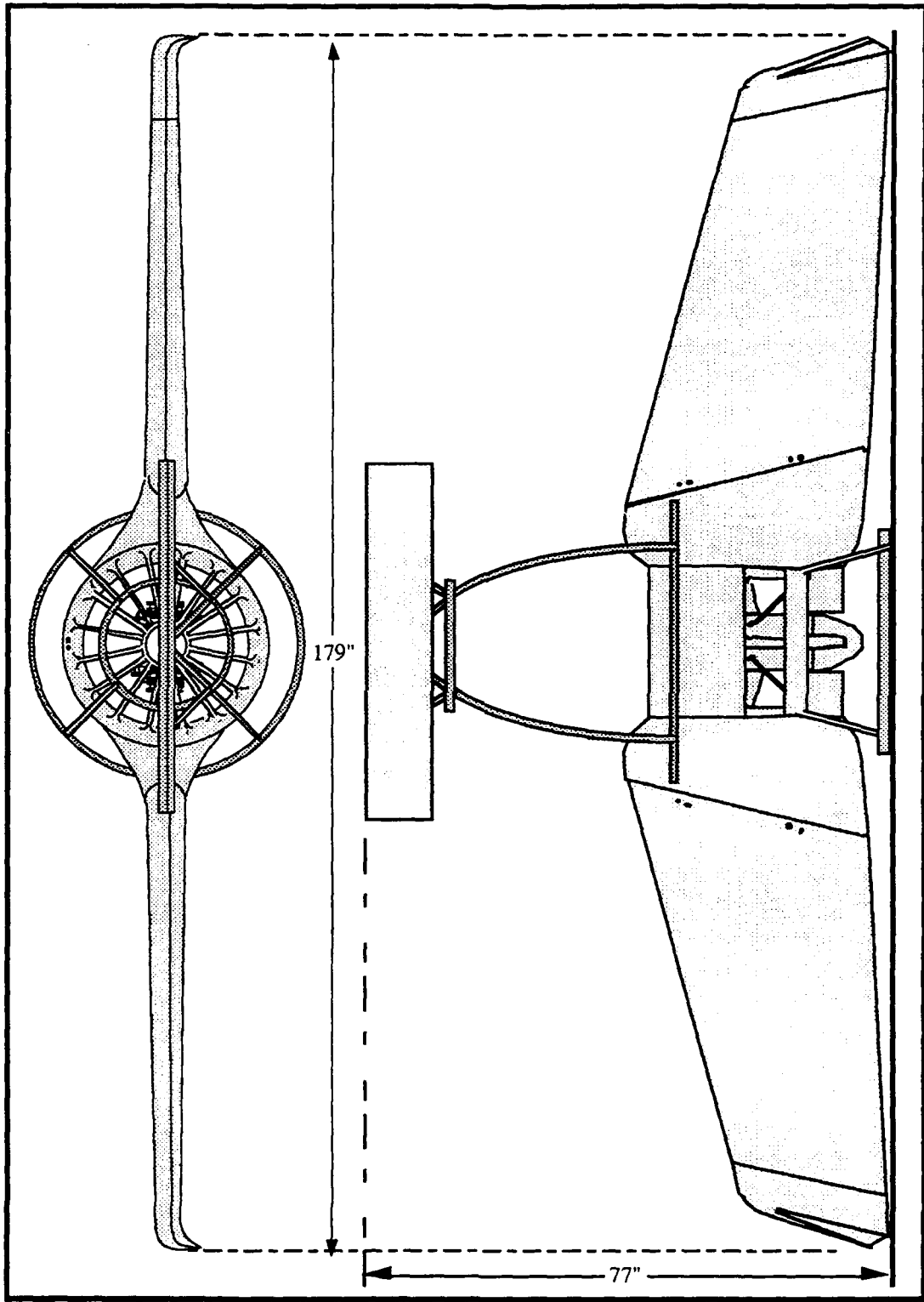
Figure 3.1. Archytas TS configuration.

attitude. The canard configuration was chosen to place the horizontal stabilizer ahead of the ducted fan. This forward location would keep the tail away from the landing ring during vertical takeoff and landing. Configuration of the forward fuselage was simplified by using the AROD roll bar. The roll bar provides increased protection during takeoff and landing as well as an excellent attachment point for the canard.

3. Landing gear

Concern for the sizing of the landing gear was given in designing the Archytas TS structural configuration. The wing sweep of 28° on the Aquila was reduced to 13° to remove the need for extending the landing gear. The significant difference in landing ring length is shown in Figure 3.3.1. With the smaller wing sweep angle the height of the duct lip was decreased from 51.75 inches to 35.5 inches. An aerodynamic improvement was also gained with the reduced sweep.

4. Shoulder joints

To connect the Aquila wings to the AROD duct an additional structure, termed shoulder joints for this discussion, was required. These shoulder joints were designed to match the end ribs of the Aquila wings and allow for removal of the wing sections for transportation and storage. Forward and aft carry-through spars were located within the shoulder joints to support forces and moments created during flight. The shoulder joints were designed to cover one quarter of the duct circumference each to allow two of the four original AROD outer duct skins to be re-attached to the upper and lower surfaces of the duct.
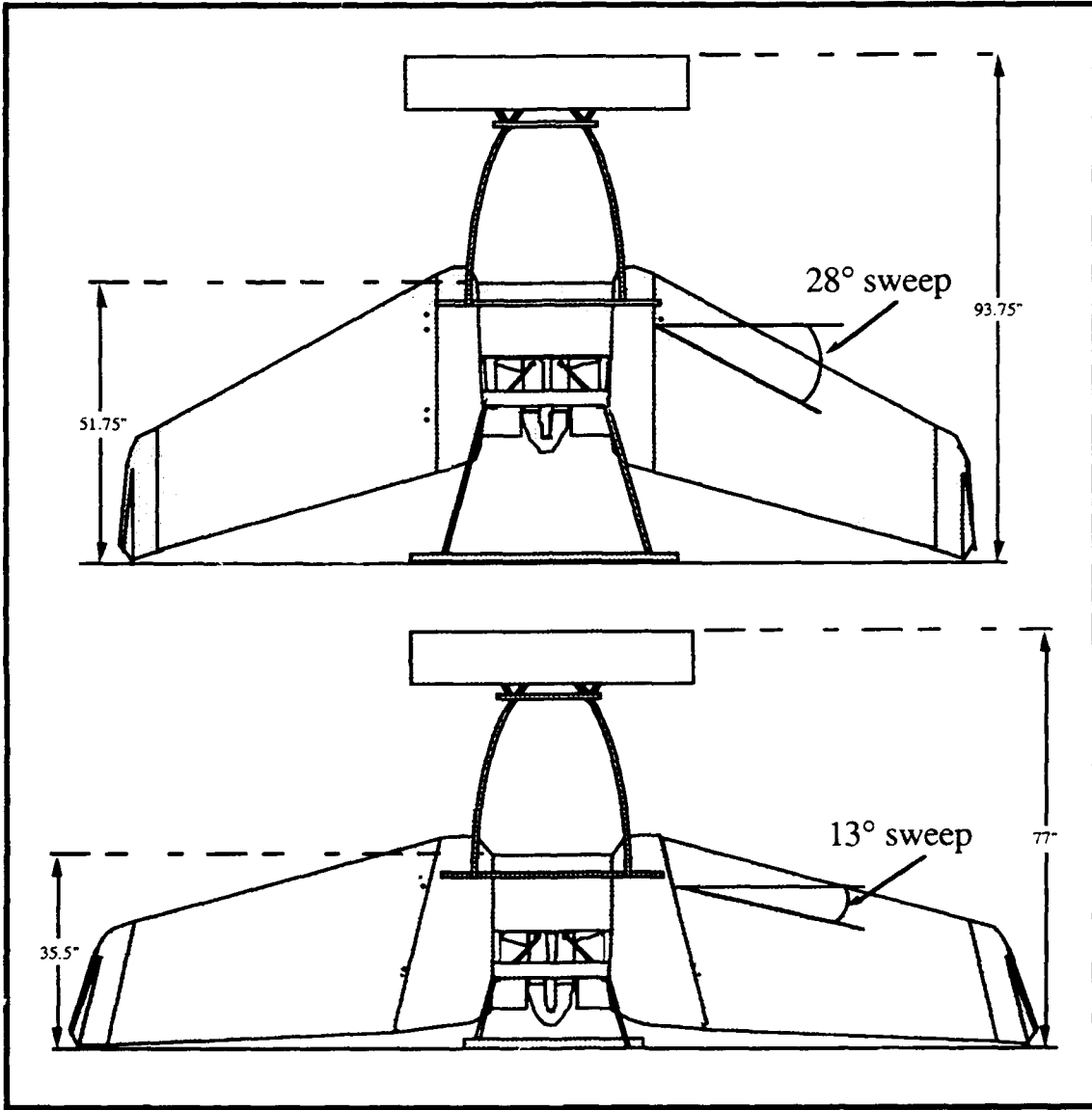
Figure 3.3.1 Effects of wing sweep angle.

IV. SPAR DESIGN

A. DESIGN PROCESS

A structural modification was necessary to attach the Aquila wings to the AROD duct.   Four primary factors were considered in the development of the spar.

1.) Structural support for a 120 lb. airframe at 8 g's.

2.) Minimal addition of any exposed frontal area that would increase profile drag.

3.) Sufficient faring of the spar to reduce any adverse wing-body interference.

4.) Composite construction to increase the strength over an equivalent weight metal structure.

The carry-through spar was designed with ring frames [Ref. 9, p.163] to allow the spar structure to pass around the circumference of the AROD without interfering with the airflow through the duct.   Forward and aft cai.y-through spars were configured to connect with the forward and aft wing spars of the Aquila wing.

The forward spar was sized to fit within the space available between the inner and outer skins of the AROD duct.   This design completely enclosed the upper and lower portions of the spar from any airflow around the duct.   The inside diameter of the spar was bonded to the inner duct skin to provide greater structural integrity.   The increased thickness of the duct available at the forward location allowed for a thicker spar.   The forward spar is 2.5 inches in average thickness and has a 1-inch width.   The forward spar did not require a larger width due to the greater thickness available.   The aft spar was designed around

the outer extension of the duct ribs that support the control vanes. The AROD provided no additional structure to which to bond the aft spar and conceal it from the airflow. Therefore, the aft spar was kept to a maximum thickness of 1 inch from the inner to outer diameter to decrease the frontal area. The spar width was increased to 2 inches to account for the smaller thickness.

Initial design of the spar structure involved constructing a 1/6-scale model [Fig. 4.1]. The model allowed visualization of the wing fillet design that would be necessary to efficiently blend the wing-duct connection. The typical wing fillet with a radius of about 10% of the root chord [Ref. 9, p.148] was increased for the Archytas TS. The fillet in this case was required to house the spar which relied on a greater thickness to carry the bending moment around the duct. The dimension for the model were selected to maintain the correct wing sweep and incidence angle. The model was constructed from a closed-cell blue polystyrene foam and the fillet was carved out to create a shape that was modified from the Aquila wing airfoil coordinates given in Appendix A. A smooth shape was determined that would allow air to travel smoothly from the leading edge to the trailing edge without any sharp disruptions in the airflow. The spar positions were located on the model and the forward and aft spar cross sections were cut out. The spar cross sections were used to determine a planform for the full-size spars that could be faired smoothly into the duct. The configuration of the full-size spars is shown in Figure 4.2.

The required dimensions for the full-size spars were calculated and used to build a finite element model. The locations of the node points are shown in Figure 4.3. Analysis of the spar structure used the MSC/pal2 finite element analysis program produced by the MacNeal-Schwender Corporation. The model

18

Forward Spar

AROD
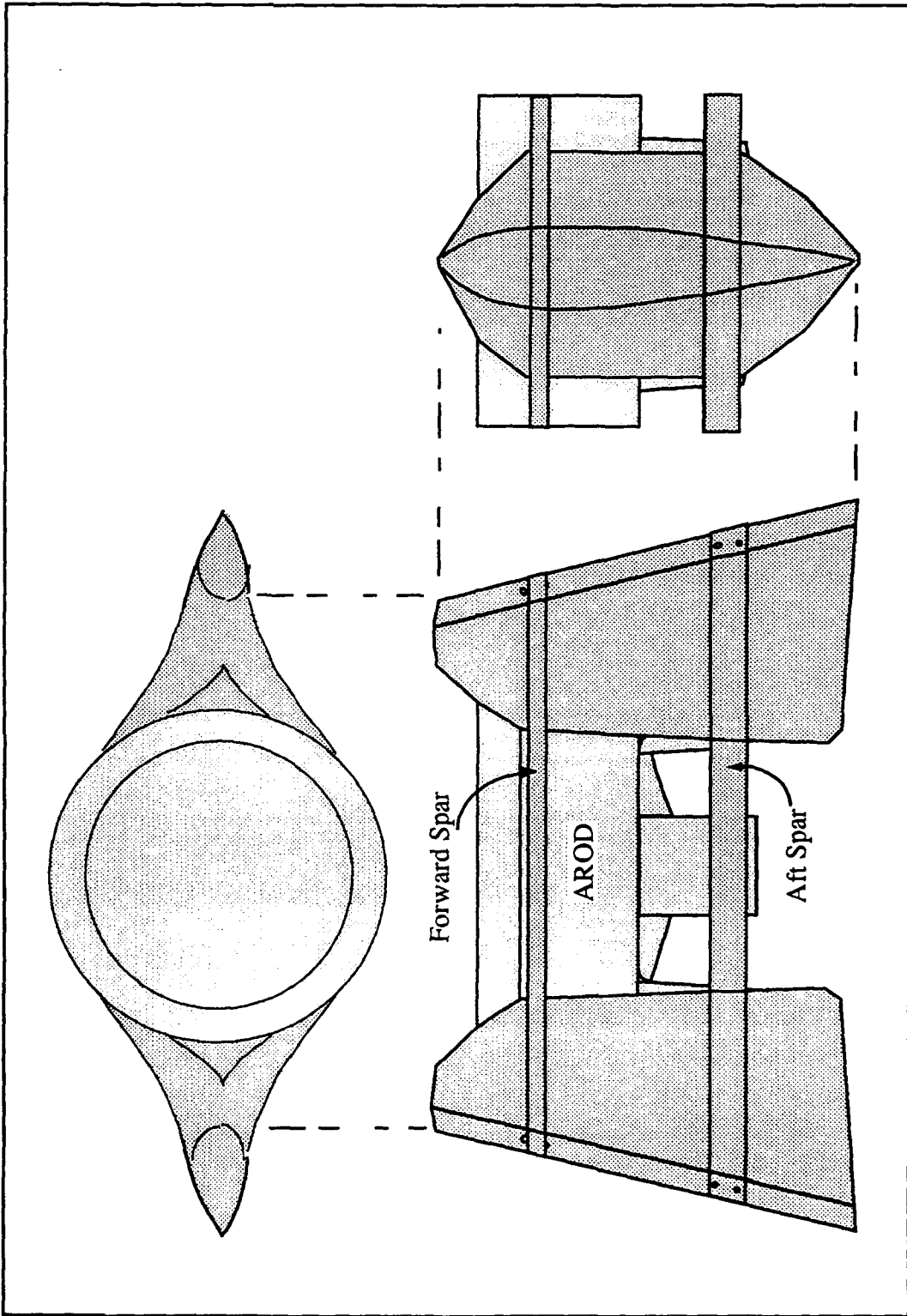
Aft Spar

Figure 4.1. Archytas foam model.
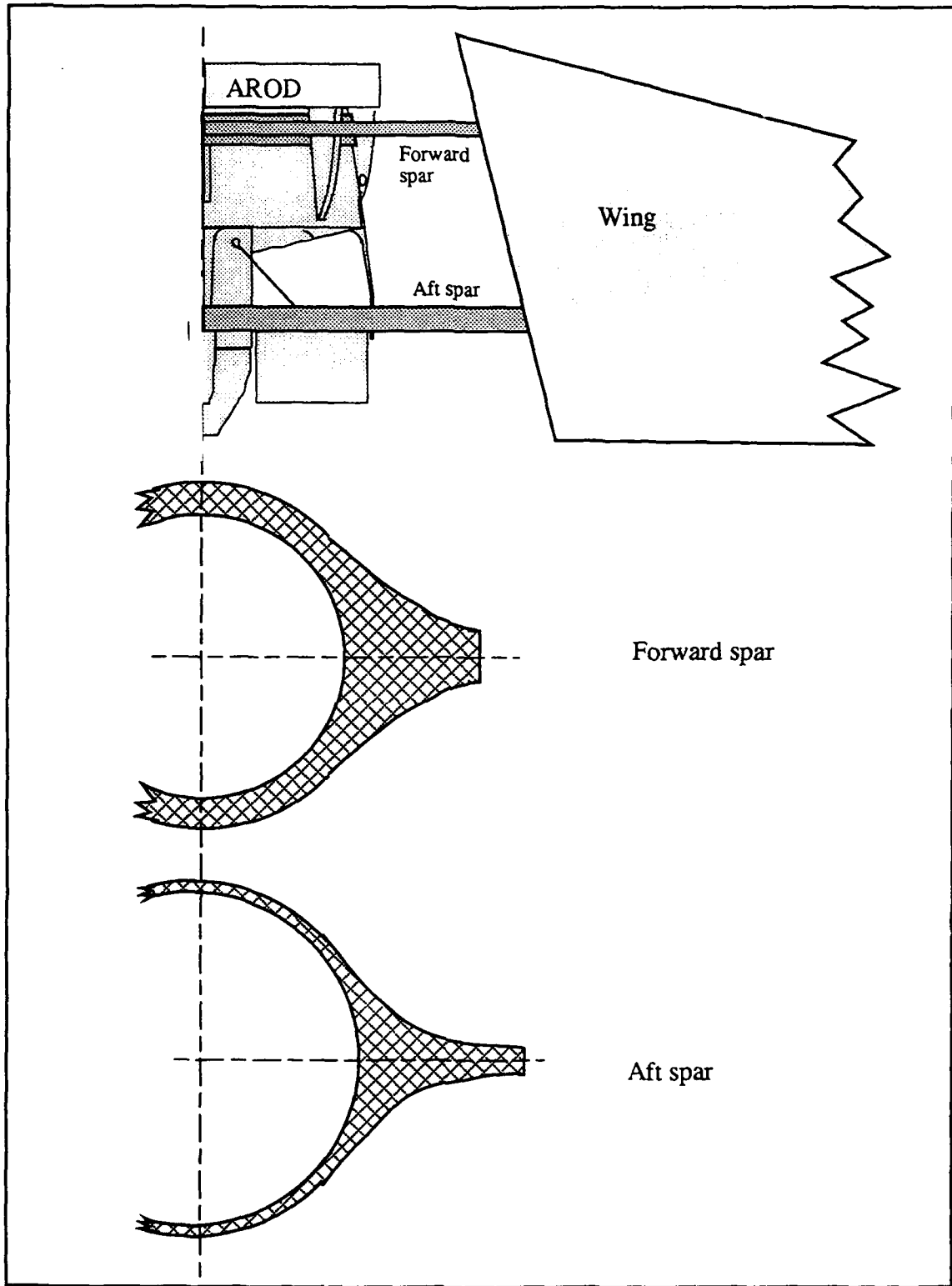
Figure 4.2. Full size spar configuration.
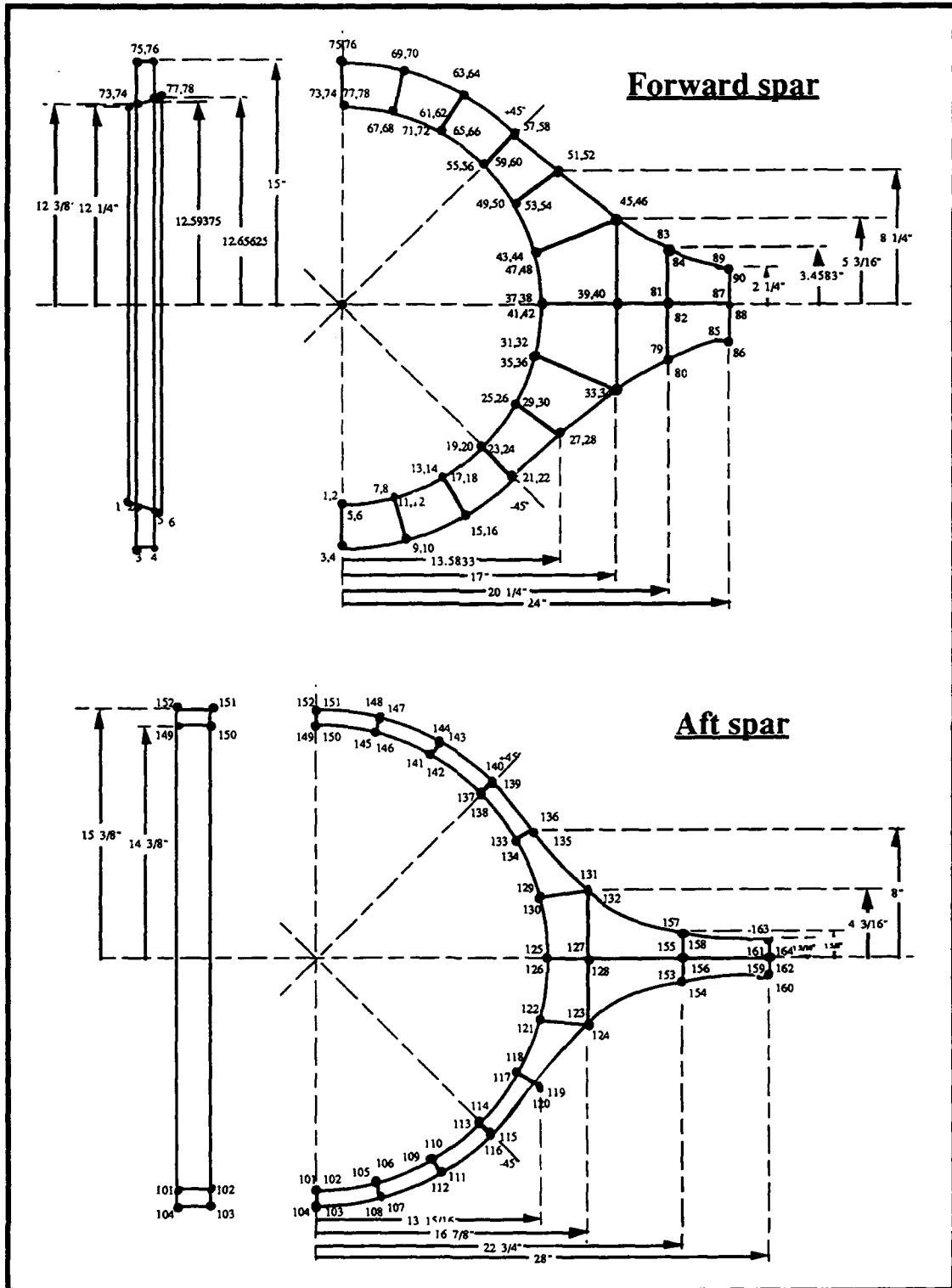
Figure 4.3. Forward and aft spar nodal point locations.

file and the nodal point locations are given in Appendix B. MSC/pal2 contains a composites module for analyzing quadrilateral elements constructed from composite laminates. Classical lamination theory is used by MSC/pal2 to compute the results for a laminate with up to 200 plies and ten different materials [Ref. 10, p.1.1].

B. MATERIAL SELECTION

The spars were built using moldless composite sandwich construction. This technique used a foam core with a composite laminate hand laid on the shear web and spar caps.

1. Core

The spar core was made from 2 lb./cu. ft. urethane foam. Urethane was selected because it is relatively inexpensive, extremely easy to cut and shape and bonds well with epoxy matrix adhesive. The foam construction considerably minimized the waste generated during the core fabrication. The cores for both full length spars and the half-span test spars were built from segments cut from a single 4' x 8' sheet of 1-inch-thick urethane foam [Fig. 4.1.1]. This involved cutting single pieces for the forward spar and two pieces for each position on the aft spar to built up the 2-inch width. Additional foam blocks were cut to construct a half span forward and aft spar for load testing. The foam segments were cut from the urethane sheet with a hacksaw blade. The edges were planed square to produce a good glue joint. The foam pieces were glued together with a micro-slurry mixture of 50% microspheres and 50% epoxy resin [Ref. 11, p.36].
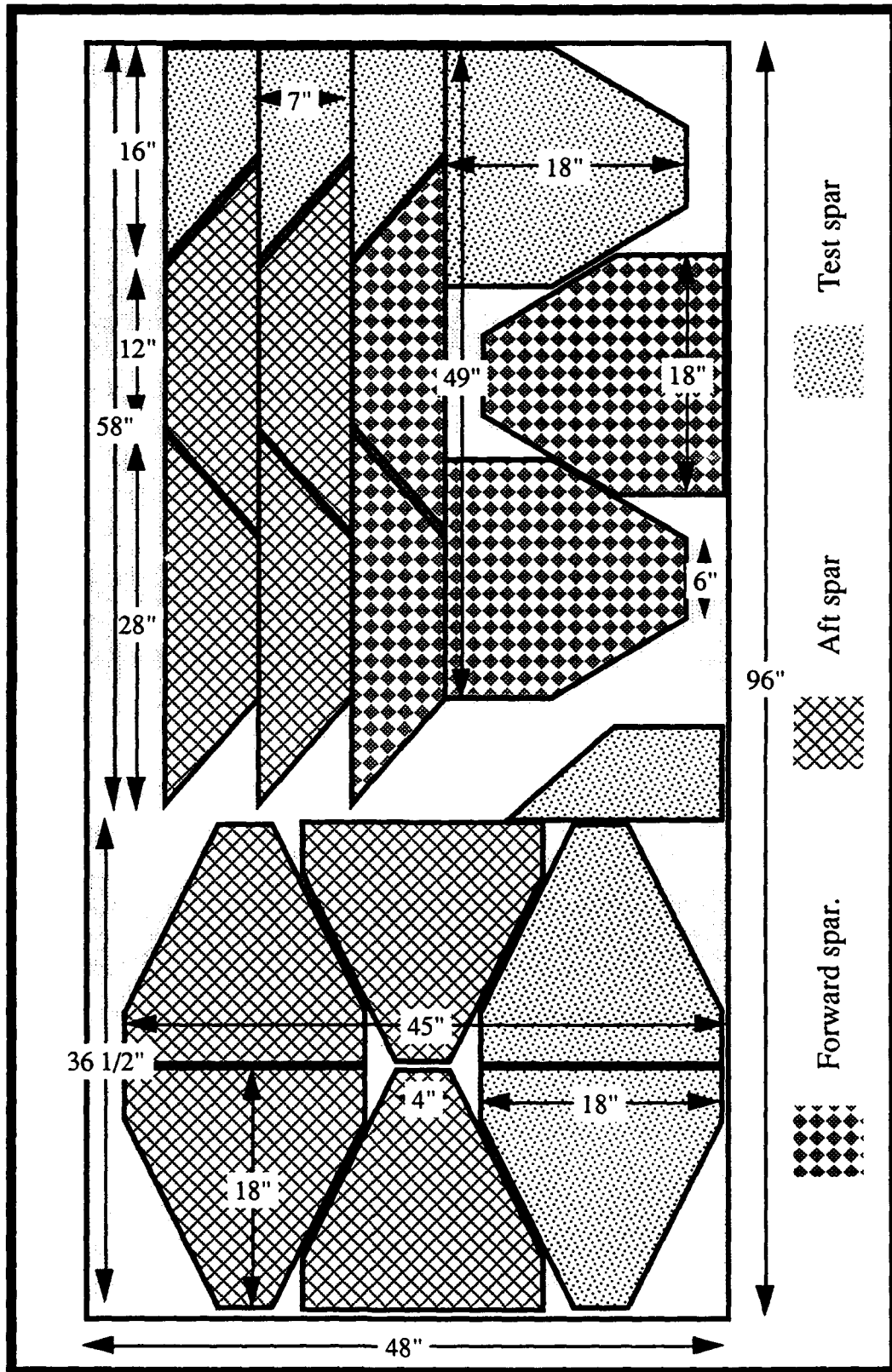
Figure 4.1.1. Foam core cutouts.

2. Adhesive

The adhesive used to bond the composite fibers together and attach them to the core is technically referred to as the matrix. The matrix used on the Archytas TS spar is Safe-T-Poxy® two-part epoxy manufactured by Hexcel Corporation. A ratio by weight of 100 parts resin to 48 parts hardener was used to mix the epoxy. Cure time for the epoxy is 10 hours to touch and 24 hours before sanding. The material properties for epoxy are listed in Table 4.2.1.

Table 4.2.1 MATRIX PROPERTIES.

Matrix	E_1, psi	E_2, psi	ν_{12}	Tensile strength	% elongation
Epoxy	0.62×10^6	0.62×10^6	0.34	8×10^3 psi	6.0

3. Reinforcement fiber

Three types of fiber were used to construct the laminates: E-glass, S-glass and graphite. E-glass is an older form of fiber that is commonly found is woven fiberglass cloths. The shear webs were constructed from an Owens-Corning woven E-glass cloth. The fabric is a 7725 twill weave that is commonly used in homebuilt aircraft. Twill was chosen because it has greater strength properties over a plain weave for the same fabric weight and amount of fibers. This is because material properties are lost by curving of the fibers in the weaving process. Figure 4.2.1 compares a twill weave with a plain weave fabric. It can be seen that fibers woven in a twill do not cross over each other as often as in a plain weave for a given length of fabric.

The unidirectional fiberglass used in the Archytas TS is Orcoweb S-500 manufactured by Orcon Corporation. It serves as the primary structural fiber in the spar caps because its strength properties are all oriented in a single direction.

Unidirectional fibers do not have any weaving crimps and have not been weakened by abrasive weaving processes. This material is constructed with Owens-Corning S-2® glass. Orcoweb S-500 fibers are held together by a single cross fiber at 1.5-inch spacing that is bonded with a thin layer of adhesive. S-glass is stronger and stiffer and weighs less than E-glass and is ideally suited for low-cost, high-strength, aerospace applications. [Ref. 13]

| Plain weave | Twill weave |
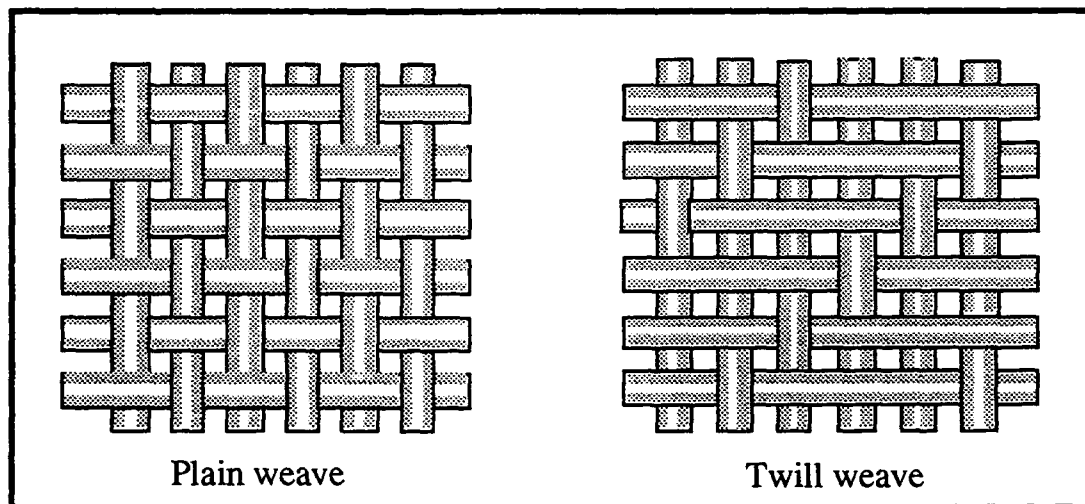
Figure 4.3.1. Types of weaves.

Graphite was used at the locations on the spar that required greater material properties than those available with S-glass. Graphite provides maximum stiffness (high modulus) and extremely high compressive and tensile strengths at a very low weight. The use of graphite falls into area of advance composites. The graphite used on the Archytas TS is manufactured by Hexcel. The fibers are held together by a widely space cross woven glass fiber. The material properties of E-glass, S-glass, and graphite are shown in Table 4.3.1.

Table 4.3.1 FIBER PROPERTIES.

Fiber	E_1, x 10^6	E_2 x 10^6	G_{12} x 10^6	υ_{12}	Tensile strength	% elongation
E-glass	10.5 psi	10.5 psi	4.37 psi	0.2	250 x 10^3 psi	2.4
S-glass	12.6 psi	12.6 psi	5.17 psi	0.2	360 x 10^3 psi	2.9
Graphite	32 psi	2 psi	2 psi	0.2	360 x 10^3 psi	1.1

4. Laminate design

The laminates were designed using classical lamination theory [Ref. 12, pp.147]. Laminate requirements were identified from the loads to be applied to the spar during flight at 8 g's with a minimum safety factor of two. Forces and moments were related to strains and curvatures by

$$
\begin{bmatrix} N_x \\ N_y \\ N_{xy} \\ L \\ M_x \\ M_y \\ M_{xy} \end{bmatrix} = \begin{bmatrix} A_{11} & A_{12} & A_{16} & M & B_{11} & B_{12} & B_{16} \\ A_{12} & A_{22} & A_{26} & M & B_{12} & B_{22} & B_{26} \\ A_{16} & A_{26} & A_{66} & M & B_{16} & B_{26} & B_{66} \\ L & L & L & M & L & L & L \\ B_{11} & B_{12} & B_{16} & M & D_{11} & D_{12} & D_{16} \\ B_{12} & B_{22} & B_{26} & M & D_{12} & D_{22} & D_{26} \\ B_{16} & B_{26} & B_{66} & M & D_{16} & D_{26} & D_{66} \end{bmatrix} \begin{bmatrix} \varepsilon_x \\ \varepsilon_y \\ \varepsilon_{xy} \\ L \\ \kappa_x \\ \kappa_y \\ \kappa_{xy} \end{bmatrix}
$$

where N and M are the loads and moments, A, B and D are the constituent material stiffness matrices, and ε and κ are the strains and curvatures [Ref. 10, p.6-6]. The A, B and D values for a laminate constitute what is referred to as the 'ABD matrix'. The values for the ABD matrix were obtained from the transformed reduced stiffness matrix, $\overline{Q}_{ij}$, for each laminate.

26

$$A_{ij} = \sum_{k=1}^{n+1} \left(\overline{Q}_{ij}\right)_k \left(h_k - h_{k-1}\right)$$

$$B_{ij} = \frac{1}{2} \sum_{k=1}^{n+1} \left(\overline{Q}_{ij}\right)_k \left(h_k^2 - h_{k-1}^2\right)$$

$$D_{ij} = \frac{1}{3} \sum_{k=1}^{n+1} \left(\overline{Q}_{ij}\right)_k \left(h_k^3 - h_{k-1}^3\right)$$

The transformed reduced stiffness matrix took into account the ply angle for each laminate [Ref. 10, p.6-4] where

$$\overline{Q}_{11} = Q_{11}\cos^4\beta + 2(Q_{12} + 2Q_{66})\sin^2\beta\cos^2\beta + Q_{22}\sin^4\beta$$

$$\overline{Q}_{22} = Q_{11}\sin^4\beta + 2(Q_{12} + 2Q_{66})\sin^2\beta\cos^2\beta + Q_{22}\cos^4\beta$$

$$\overline{Q}_{12} = (Q_{11} + Q_{22} - 4Q_{66})\sin^2\beta\cos^2\beta + Q_{12}(\sin^4\beta + \cos^4\beta)$$

$$\overline{Q}_{66} = (Q_{11} + Q_{22} - 2Q_{12} - 2Q_{66})\sin^2\beta\cos^2\beta + Q_{66}(\sin^4\beta + \cos^4\beta)$$

$$\overline{Q}_{16} = (Q_{11} - Q_{12} - 2Q_{66})\sin\beta\cos^3\beta + (Q_{12} - Q_{22} + 2Q_{66})\sin^3\beta\cos\beta$$

$$\overline{Q}_{26} = (Q_{11} - Q_{12} - 2Q_{66})\sin^3\beta\cos\beta + (Q_{12} - Q_{22} + 2Q_{66})\sin\beta\cos^3\beta$$

The reduced stiffness matrix, Q_{ij}, for each laminate was derived from the ply material properties [Ref. 10, p.6-3].

$$Q_{11} = \frac{E_1}{\left(1 - \upsilon_{12} * \upsilon_{21}\right)}$$

$$Q_{22} = \frac{E_2}{\left(1 - \upsilon_{12} * \upsilon_{21}\right)}$$

$$Q_{12} = \frac{\upsilon_{21} * E_1}{\left(1 - \upsilon_{12} * \upsilon_{21}\right)}$$

$$Q_{66} = G_{12}$$

The ply material properties are calculated from the fiber and matrix properties that create the laminate [Ref. 10, p.6-13].

27

$$E_1 = E_{1f}F_V + E_{1m}(1 - F_V)$$

$$E_2 = E_{2m} \frac{\left(1 + \dfrac{E_{2f}/E_{2m} - 1}{E_{2f}/E_{2m} + 1}F_V\right)}{\dfrac{E_{2f}/E_{2m} - 1}{E_{2f}/E_{2m} + 1}}$$

$$\upsilon_{12} = \upsilon_{1f}F_V + \upsilon_{1m}(1 - F_V)$$

$$G_{12} = \frac{G_{12m}\left(G_{12f}(1 + F_V) + G_{12m}(1 - F_V)\right)}{G_{12f}(1 - F_V) + G_{12m}(1 - F_V)}$$

where F_V is the fiber volume of the laminate and the subscripts m and f refer to the matrix and fiber properties, respectively.

5. Shear web

Laminate design was similar for the shear web for both the forward and aft spars. Any coupling between extension and bending of the shear web was not desired. If coupling occurred, any shear force applied to the spar would result in a twisting of the shear web laminate. To avoid coupling the shear web was formed from layers that were symmetric about the laminate midplane with opposite signs of ply angle orientation, $\pm\beta$. This simplified the ABD matrix by setting $A_{16}=A_{26}=0$ and $[B_{ij}]=0$ [Ref. 12, p.165].

$$\begin{bmatrix} N_x \\ N_y \\ N_{xy} \end{bmatrix} = \begin{bmatrix} A_{11} & A_{12} & 0 \\ A_{12} & A_{11} & 0 \\ 0 & 0 & A_{66} \end{bmatrix} \begin{bmatrix} \varepsilon_x \\ \varepsilon_y \\ \varepsilon_{xy} \end{bmatrix} \text{ and } \begin{bmatrix} M_x \\ M_y \\ M_{xy} \end{bmatrix} = \begin{bmatrix} D_{11} & D_{12} & 0 \\ D_{12} & D_{11} & 0 \\ 0 & 0 & D_{66} \end{bmatrix} \begin{bmatrix} \kappa_x \\ \kappa_y \\ \kappa_{xy} \end{bmatrix}$$

To minimize the laminate shear strain, ε_{xy}, it was desired to maximize the A_{66} value in the ABD matrix. This calculation required the determination of the optimum ply angle, β, which would result in the largest values of $\overline{Q}_{66}$ in the transformed reduced stiffness matrix. With Q_{11}, Q_{22}, Q_{12} and Q_{66} values fixed from the material properties, the angle, β, was varied from -90° to +90°. Figure

4.5.1 reveals that the maximum values were obtained for $\beta = \pm 45°$. The program used to determine the ply angle optimization was written in MATLAB®. The code is given in Appendix C. This ply angle agrees with the industry standard to orient material properties at $\pm 45°$ to the longitudinal axis to provide the highest shear properties [Ref. 14, p.386]. The 7725 twill weave fiberglass was ideal for application to the shear web. The fabric oriented at $\pm 45°$ created a regular symmetric angle-ply laminate that had optimal shear properties. An individual thickness, t, of woven fabric was modeled in MSC/pal2 by placing four layers of unidirectional material of thickness t/4 at $\pm 45°$ orientation. The ply properties, laminate layup, and laminate properties are listed in Appendix C. The laminate thickness for the shear web varied at different locations across the spar. The thickness was chosen to minimize the stress concentration caused from the flight loads. The laminate layup for the shear web is shown in Table 4.5.1. The location of each laminate corresponds with the placement shown in Figure 4.5.2.
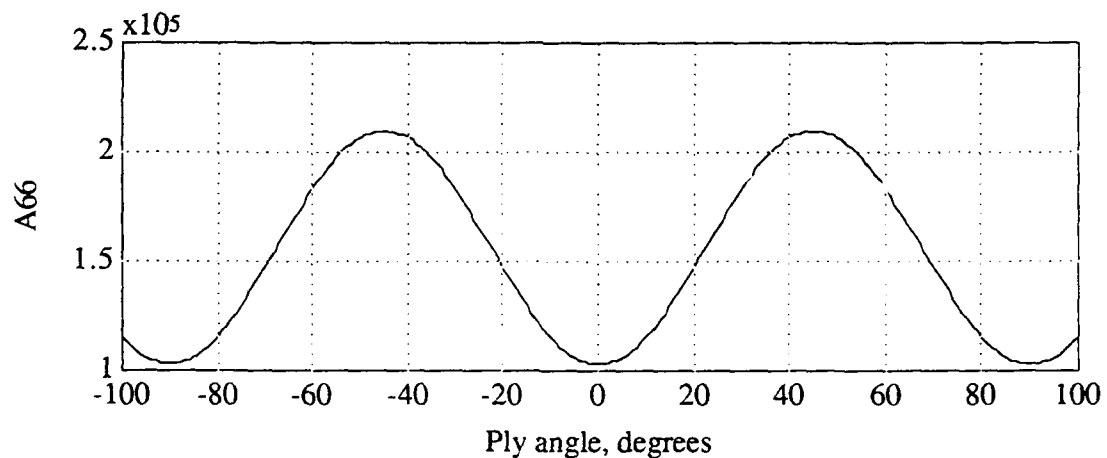
Figure 4.5.1. Shear web optimization.

Table 4.5.1. SHEAR WEB LAMINATE THICKNESS.

Spar	Location	Layers
Forward	A	3
	B	4
	C	5
Aft	D	4
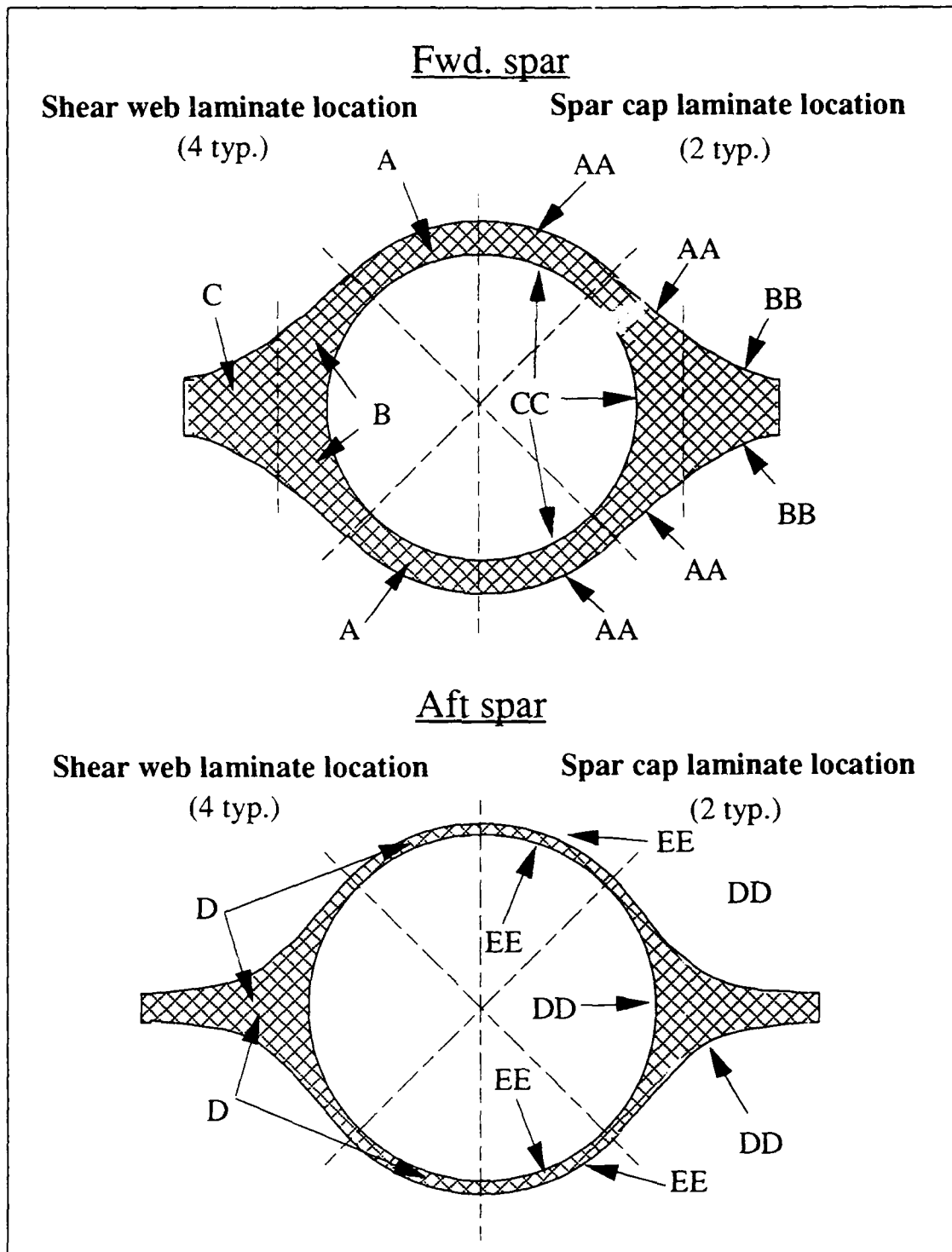
Figure 4.5.2. Spar laminate location.

6. Spar cap

The laminates for the spar caps were similar in design, but differed in material composition. The forward spar caps were required to carry more of the flight loads. Additional stiffness and strength were designed into the forward spar caps by increasing the laminate thickness and adding more layers of carbon fiber at critical locations. Bending stiffness is controlled by the D_{ij} values in the ABD matrix. The carbon fibers were located at the outer layers of the laminate. This location provided the greatest effect of $\left(h_k^3 - h_{k-1}^3\right)$ on creating larger values of D_{ij} when looking at the entire spar height as a single laminate.

The optimum ply angle was determined in a similar manner as that for the shear web. For the spar caps the flight loads would create an N_x value in the ABD matrix. This force caused compression on the upper spar cap and tension on the lower spar cap. A nonsymmetric laminate with multiple specially orthotropic layers was created by placing the graphite on the outside plys with all of the principal material directions aligned with the laminate axis [Ref. 12, p.162]. The individual spar caps were not considered symmetric because of the difference in material properties for graphite and S-glass; however, the upper and lower spar caps with the foam core in between created a symmetric spar. The ABD matrix for an individual spar cap took the form of

$$
\begin{bmatrix} N_x \\ N_y \\ N_{xy} \\ \cdots \\ M_x \\ M_y \\ M_{xy} \end{bmatrix} = \begin{bmatrix} A_{11} & A_{12} & 0 & M & B_{11} & B_{12} & 0 \\ A_{12} & A_{22} & 0 & M & B_{12} & B_{22} & 0 \\ 0 & 0 & A_{66} & M & 0 & 0 & B_{66} \\ L & L & L & M & L & L & L \\ B_{11} & B_{12} & 0 & M & D_{11} & D_{12} & 0 \\ B_{12} & B_{22} & 0 & M & D_{12} & D_{22} & 0 \\ 0 & 0 & B_{66} & M & 0 & 0 & D_{66} \end{bmatrix} \begin{bmatrix} \varepsilon_x \\ \varepsilon_y \\ \varepsilon_{xy} \\ L \\ \kappa_x \\ \kappa_y \\ \kappa_{xy} \end{bmatrix}
$$

To minimize the normal strain, ε_x , due to N_x , large values of A_{11} and A_{12} were desired. Figure 4.6.1 shows that the maximum values were obtained for $\beta=0°$.

The laminate thickness for the spar caps varied at different locations across the spar. The thickness was chosen to minimize the stress concentration caused from the flight loads. The laminate layup for the spar caps is given in Table 4.6.1 The location of each laminate corresponds with the placement shown in Figure 4.5.2. Unlike the shear web, the spar cap layers were modeled directly in MSC/pal2 as they appear in the actual laminate.
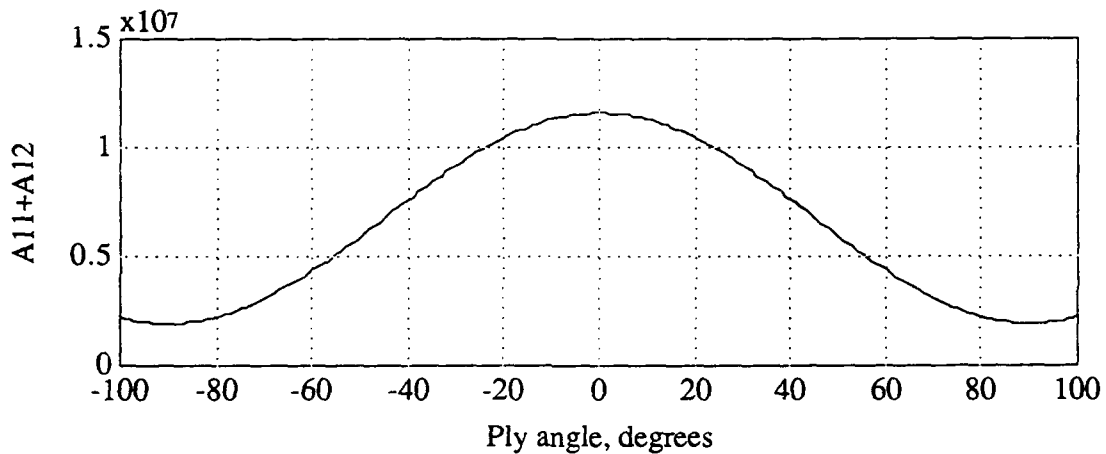
Figure 4.6.1. Spar cap ply angle optimization.

Table 4.6.1. SPAR CAP LAMINATE THICKNESS.

Spar	Location	S-glass layers	Graphite layers
Forward	AA	4	2
	BB	8	3
	CC	3	0
Aft	DD	3	1
	EE	4	2

V. TEST STAND

A. TEST STAND REQUIREMENTS

A fundamental requirement in the calculation of aircraft performance is accurate knowledge of powerplant characteristics. For a piston-driven engine, accurate knowledge of available horsepower is essential in calculating horizontal flight performance. VTOL-configured aircraft are also concerned with vertical flight performance, similar to helicopters, and require information on maximum thrust available. Procedures used in the power plant analysis for the Archytas TDF are described in Reference 5. The test stand for the TDF design consisted of two main components. One portion allowed for determination of the horsepower by measuring the torque created by the engine over a range of RPM. Static thrust output for the engine was obtained by a separate part of the test stand by attaching the entire ducted fan to a sliding tray. The sliding tray pulled on a spring scale which measured static thrust directly. In principle the equipment was sufficient; however, the following deficiencies were observed:

1. Inability to measure thrust and horsepower simultaneously.
2. Airflow blockage resulting from the thrust stand configuration.
3. Friction losses due to poor bearing surfaces for the sliding tray.
4. Inadequate size in both the torque and thrust components to support the larger powerplant for the Archytas TS.

A recommendation resulting from the Archytas TDF research was to design and construct a larger engine test stand that could accurately measure and record thrust, torque, and engine RPM [Ref. 6, p.64].

B. TEST STAND DESIGN

Initial considerations for a larger test stand began simply with a scaled-up version of the smaller configuration used for the TDF design. However, the mechanical complexity involved in constructing an efficient sliding tray to support an apparatus for measuring both torque and thrust was not desirable. The final focus was directed at a linear bearing arrangement. A linear bearing consists of numerous rows of ball bearings mounted axially along the inner circumference of the outer bearing race. These rows of ball bearings allow a highly polished, hardened steel shaft to traverse linearly through the bearing and rotate simultaneously. An arrangement of two linear bearings mounted in series along with a 16-inch shaft was salvaged from a previous NPS experiment. The equipment was restored and modified to create a test stand on which to mount the entire AROD duct. The test stand was mounted to a large base to provide *support and stability during use. Wheels mounted underneath the base could be* extended to roll the entire assembly; for engine tests, the wheels could be retracted to place the frame firmly on the ground and prevent any movement. The complete configuration of the test stand is shown in Figure 5.1.

C. TEST STAND ANALYSIS

Static analysis was performed on the load-carrying components of the test stand listed in Table 5.1 to ensure that they could withstand the loads applied with the duct in place and additional forces produced during engine run-up.

The analysis was performed using a strength-of-materials approach [Ref. 15]. The maximum normal and shear stress was calculated for each component.

Table 5.1 COMPONENT ANALYSIS.

Component	Analysis
Bearing	Static load.
Shaft	Bending, shear, torsion.
Extension	Bending, shear, torsion.
Bracket	Bending, shear, torsion.

Side View

Top View
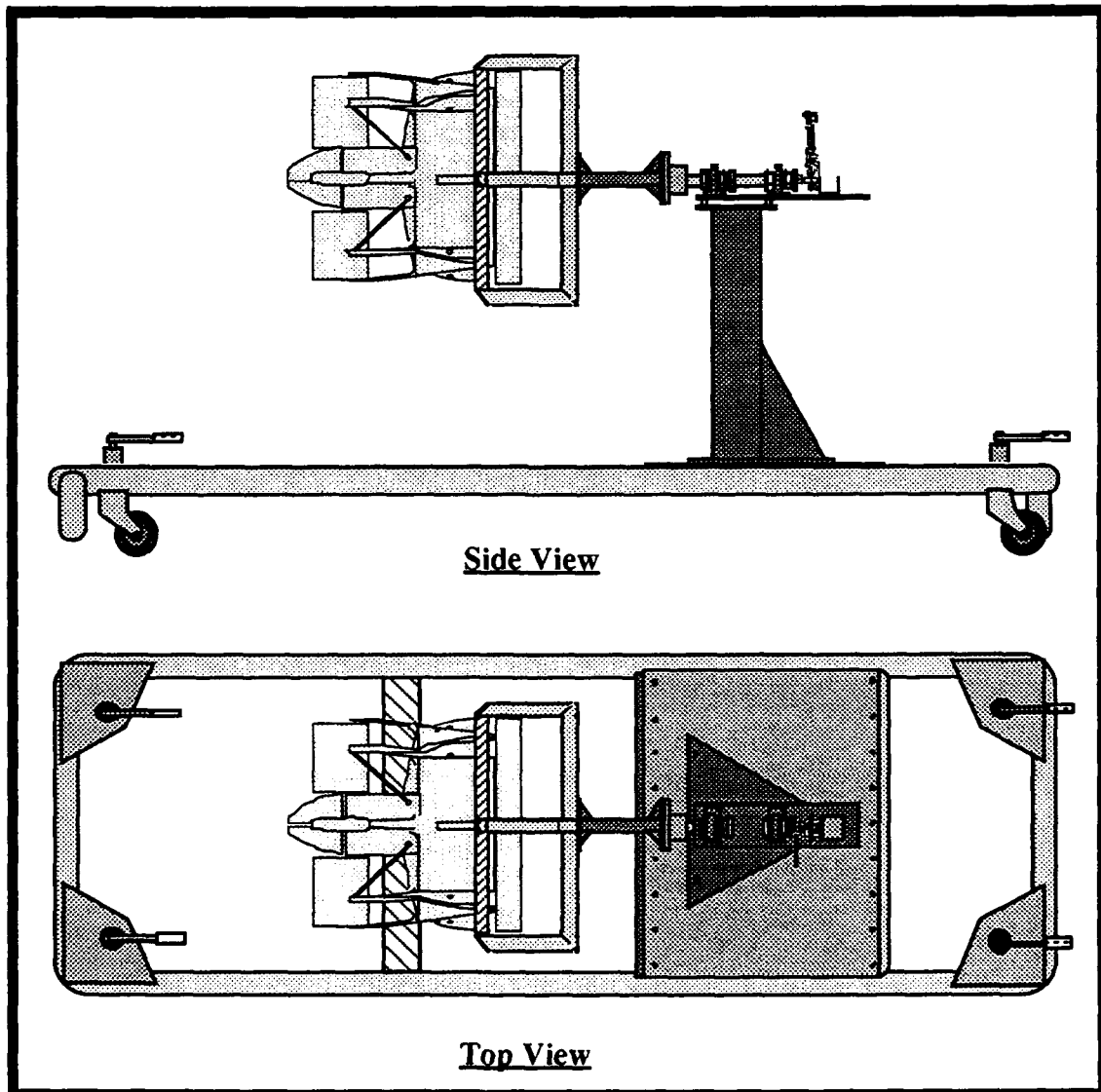
Figure 5.1. Engine test stand.

The material yield stress and the maximum stress values were applied to Von Mises' yield criterion to ensure that no component of the test stand would reach a point of yield. Calculations for the analysis of each component is given in Appendix D. The material yield stress was compared to the Von Mises' yield criterion to produce a factor of safety.

$$\text{Factor of safety} = \frac{\text{Material yield stress}}{\text{Von Mises' yield stress}}$$

The results from the analysis in Appendix D are listed in Table 5.

Table 5.2 FACTOR OF SAFETY.

Component	Material Yield Stress	Von Mises' Yield Stress	Factor of Safety
Bearings	1560 lbs.*	314.5*	5.0
Shaft	275,000 psi	6358.1 psi	43.3
Extension	36,000 psi	3479.3 psi	10.3
Bracket	37,000 psi	1008.2 psi	36.7

*Bearing normal and actual load ratings.

D. ENGINE TEST RESULTS

Engine tests were performed with the AROD mounted on the test stand. A 6-inch moment arm [App. E] was clamped to the shaft to regulate the rotation. Torque was measured with a spring mounted on the end of the moment arm. The thrust from the engine pushed on the shaft and exerted a load on an spring load cell. The throttle setting was controlled with an electric servo. Engine RPM was set with a computer controlling the throttle servo. Torque and thrust

37

readings were obtained simultaneously over the range of RPM listed in Table 5.3. Horsepower was calculated from the measured RPM using

$$Hp = Torque_{(in.\bullet lbs.)} \bullet (2\pi RPM) \bullet \left(\frac{1\ Hp}{550\ \frac{ft.\bullet lbs.}{sec.}} \right) \bullet \left(\frac{1}{60}\frac{sec.}{min.} \right) \bullet \left(\frac{1}{12}\frac{in.}{ft.} \right)$$

The test data are plotted in Figures 5.2 and 5.3.

Table 5.3. ENGINE TEST DATA.

Computer Throttle setting	Engine RPM	Thrust lbf.	Moment lbf	Horsepower
50.0	1929.0	8.0	-4.0	-0.735
55.0	2115.0	10.0	-3.0	-0.604
60.0	2210.0	13.0	-3.0	-0.631
65.0	2850.0	19.0	-1.0	-0.271
70.0	3720.0	25.0	0.0	0.000
75.0	4050.0	32.0	2.0	0.771
80.0	5160.0	56.0	6.0	2.947
85.0	5820.0	62.0	10.0	5.540
90.0	6030.0	65.0	8.0	4.592
95.0	6300.0	70.0	8.0	4.798
100.0	6630.0	73.0	6.0	3.787
105.0	6960.0	78.0	9.0	5.963
110.0	7080.0	79.0	11.0	7.414
115.0	7110.0	83.0	16.0	10.830
120.0	7380.0	88.0	20.0	14.051
125.0	7380.0	90.0	18.0	12.646
130.0	7350.0	90.0	14.0	9.796
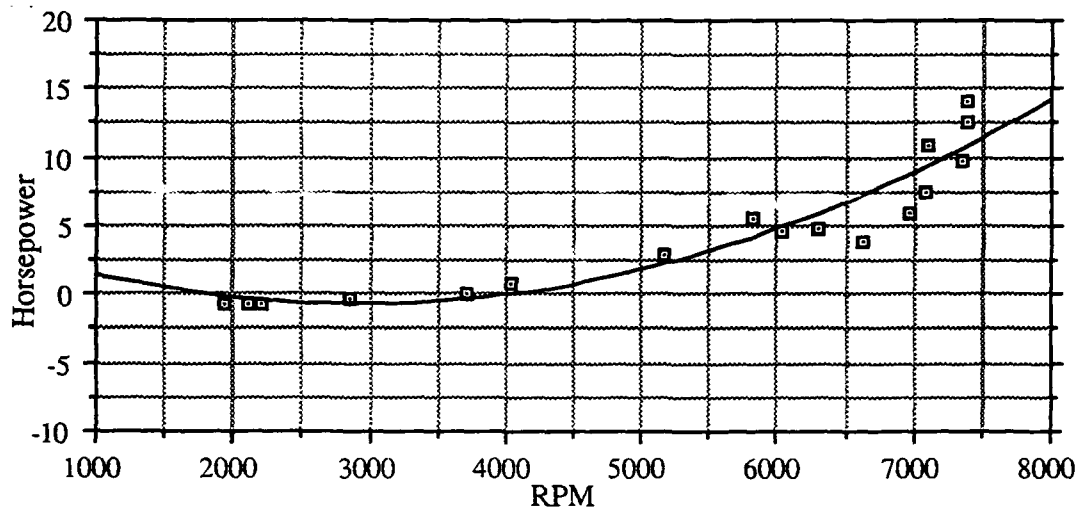
Figure 5.2. Horsepower vs. RPM.
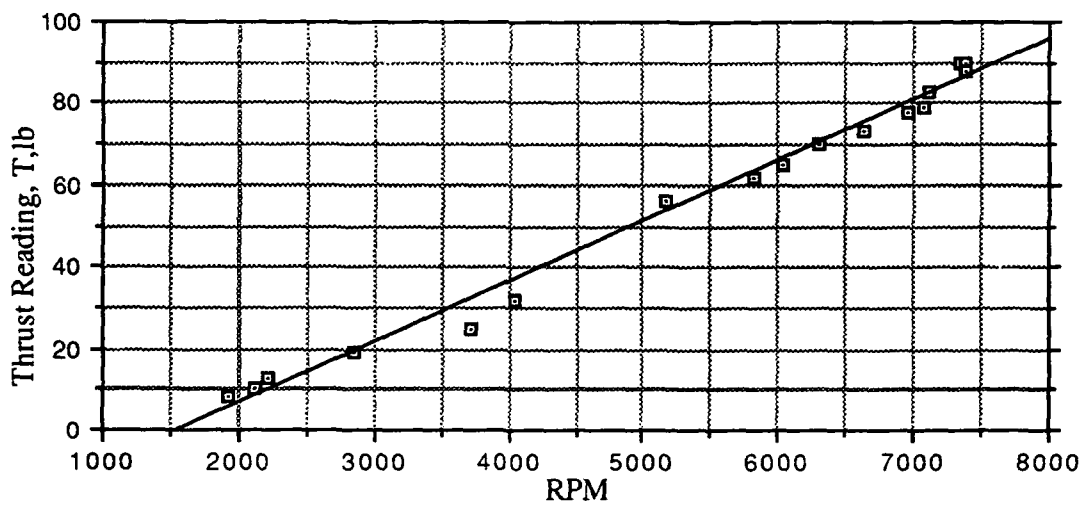
Figure 5.3. Thrust vs. RPM.

VI. CONCLUSIONS AND RECOMMENDATIONS

A. CONCLUSIONS

A full-scale VTOL Unmanned Air Vehicle was developed based on previous research on a half-scale UAV. The configuration was modified considerably from the half-scale design. The airframe was designed to incorporate the wings from a U.S. Army Aquila and the ducted fan from a U.S. Marine Corps AROD.

The goal of this research was to select a new configuration that did not require a complex duct-tilting mechanism to transition from vertical to horizontal flight. The investigation resulted in a fixed duct, tailsitter vehicle with a canard configured horizontal stabilizer.

Forward and aft carry-through spars were developed to connect the wings to the ducted fan. The spars were designed using computer finite element analysis. The material selected for the spar construction consisted of a urethane foam core and fiberglass/epoxy reinforced laminated. Carbon fiber was added to the composite in areas that require increased strength and stiffness. Laminate design was selected using finite element analysis.

An accurate knowledge of engine parameters was required to effectively begin development of the UAV. A large-scale engine test stand was designed and constructed to obtain powerplant thrust and horsepower measurements. The test stand provided attachment for the entire AROD and was supported by a linear-bearing arrangement. Engine tests that were performed indicated that a more accurate load cell for the thrust and torque measurements was required. In addition, the fixed anti-torque vanes interfered with the horsepower measurements.

B. RECOMMENDATIONS

The AROD roll bar should provide an ideal attachment point for the canard. The canard sizing should be calculated based on the fixed length of the roll bar.

The strength of the composite layup is very dependent on the construction procedures and laminate orientation, The manufacturing process can introduce excess voids or resin-rich areas that will lower the composite strength from the design limit. Load testing of the half-span test spar is vital to the design of the full-size carry-through spar to insure that the finite element design was sufficient to size the spar.

The negative horsepower measurements identified the influence that the duct had on the engine torque measurements. To obtain accurate horsepower readings it will be necessary to construct an attachment to mount just an engine on the test stand. A accurate stain-gauge load cell should be acquired to obtain accurate test stand measurements.

APPENDIX A

Table A1. WING AIRFOIL COORDINATES*.

Station	Upper Surface	Lower Surface
0.0	--	0.0
1.25	3.34	1.54
2.5	4.44	2.25
5.0	5.89	3.04
7.5	6.90	3.61
10	7.64	4.09
15	8.52	4.84
20	8.92	5.41
25	9.08	5.78
30	9.05	5.96
40	8.59	5.92
50	7.74	5.50
60	6.61	4.81
70	5.25	3.79 (modified)
80	3.73	2.43 (modified)
90	2.26 (modified)	1.00 (modified)
95	1.69 (modified)	.0239 (modified)
100	1.00 (modified)	.016 ± 0.5 (modified)

* [Ref. 6, p.82]

Table A2. KEVLAR® MATERIAL PROPERTIES.*

Material	Tension		Compression	
	Strength (ksi)	Modulus (psi)	Strength (ksi)	Modulus (psi)
Kevlar Unidirectional	170	10.1	40	10.1
Style Fabric 120	60	4.4	23	3.5
Style Fabric 281	70	4.4	26	4.0

* [Ref. 6, p.94]

Table A3. WING LAMINATE PROPERTIES*

Member	Material	Load	σ_{max} (psi)	σ_{ult} (psi)	Factor of Safety
Wing skins	Honeycomb sandwich	Compression	8880	12,000	1.35
Elevons	Honeycomb sandwich	Compression	2534	12,000	4.74
Fwd. spar	Kevlar	Compression	17,868	25,700	1.443
Aft Spar	Kevlar	Compression	14,758	25,700	1.763

* [Ref. 6, p.69]

APPENDIX B

A. MSC/PAL2 MODEL FILE

```
TITLE ARCHYTAS SPAR(MIN)
NODAL POINT LOCATIONS 3
1 12.25 -90 0.25 THROUGH 73 12.25 90 0.25 STEP 6
2 12.5 -90 0.75 THROUGH 74 12.5 90 0.75 STEP 6
5 12.59375 -90 1.75 THROUGH 77 12.59375 90 1.75 STEP 6
6 12.65625 -90 2.25 THROUGH 78 12.65625 90 2.25 STEP 6
3 15 -90 0.75 THROUGH 21 15 -45 0.75 STEP 6
57 15 45 0.75 THROUGH 75 15 90 0.75 STEP 6
4 14.96875 -90 1.75 THROUGH 22 14.96875 -45 1.75 STEP 6
58 14.96875 45 1.75 THROUGH 76 14.96875 90 1.75 STEP 6
101 14.875 -90 18.75 THROUGH 149 14.875 90 18.75 STEP 4
102 14.875 -90 20.75 THROUGH 150 14.875 90 20.75 STEP 4
103 15.875 -90 20.75 THROUGH 115 15.875 -45 20.75 STEP 4
139 15.875 45 0.75 THROUGH 151 15.875 90 20.75 STEP 4
104 15.875 -90 18.75 THROUGH 116 15.875 -45 18.75 STEP 4
140 15.875 45 1 8.75 THROUGH 152 15.875 90 18.75 STEP 4
NODAL POINT LOCATIONS 1
33 17 -5.1875 0.75 THROUGH 45 17 5.1875 0.75 STEP 6
34 17 -5.1875 1.75 THROUGH 46 17 5.1875 1.75 STEP 6
79 20.25 -3.4583 0.75 THROUGH 83 20.25 3.4583 0.75 STEP 2
80 20.25 -3.4583 1.75 THROUGH 84 20.25 3.4583 1.75 STEP 2
85 23.75 -2.25 0.75 THROUGH 89 23.75 2.25 0.75 STEP 2
86 24.0 -2.25 1.75 THROUGH 90 24.0 2.25 1.75 STEP 2
27 13.5833 -8.25 0.75 THROUGH 51 13.5833 8.25 0.75 STEP 24
28 13.5833 -8.25 1.75 THROUGH 52 13.5833 8.25 1.75 STEP 24
123 16.875 -4.1875 20.75 THROUGH 131 16.875 4.1875 20.75 STEP 4
124 16.875 -4.1875 18.75 THROUGH 132 16.875 4.1875 18.75 STEP 4
153 22.75 -1.626 20.75 THROUGH 157 22.75 1.625 20.75 STEP 2
154 22.75 -1.625 18.75 THROUGH 158 22.75 1.625 18.75 STEP 2
159 28 -1.1875 20.75 THROUGH 163 28 1.1875 20.75 STEP 2
160 28 -1.1875 18.75 THROUGH 164 28 1.1875 18.75 STEP 2
119 13.9375 -8 20.75 THROUGH 135 13.9375 8 20.75 STEP 16
120 13.9375 -8 18.75 THROUGH 136 13.9375 8 18.75 STEP 16
301 21.75 .5 -7 THROUGH 302 21.75 -.5 -7
307 30.428 .5 28 THROUGH 308 30.428 -.5 28
309 47.482 .5 0 THROUGH 310 47.482 -.5 0
```

311 47.482 2.125 6.263 THROUGH 312 47.482 -2.125 6.263
313 47.482 2.125 7.221 THROUGH 314 47.482 -2.125 7.221
315 47.482 1.25 19.025 THROUGH 316 47.482 -1.25 19.025
317 47.482 1.25 21.025 THROUGH 318 47.482 -1.25 21.025
319 47.482 0.5 28.694 THROUGH 320 47.482 -0.5 28.482
C
C FWD SPAR, SHEAR WEB, (+45 TO +90) AND (-45 TO -90).
C
LAMINATE DATABASE LAM.ARC
MATERIAL COMPOSITE 16,2
QUADRILATERAL PLATE TYPE 1 3
GENERATE CONNECTS 1 19 21 6 1
GENERATE CONNECTS 4 22 24 6 1
GENERATE CONNECTS 55 73 75 6 1
GENERATE CONNECTS 58 76 78 6 1
C
C FWD SPAR, SHEAR WEB, +45 TO -45.
C
LAMINATE DATABASE LAM.ARC
MATERIAL COMPOSITE 18,2
QUADRILATERIAL PLATE TYPE 1 3
GENERATE CONNECTS 19 31 33 6 1
GENERATE CONNECTS 43 55 57 6 1
GENERATE CONNECTS 22 34 36 6 1
GENERATE CONNECTS 46 58 60 6 1
GENERATE CONNECTS 31 43 44 6 1
GENERATE CONNECTS 32 33 45 1 6
GENERATE CONNECTS 35 34 46 1 6
GENERATE CONNECTS 35 47 48 6 1
LAMINATE DATABASE LAM.ARC
MATERIAL COMPOSITE 20,2
QUADRILATERIAL PLATE TYPE 1 3
GENERATE CONNECTS 79 86 89 6 2
GENERATE CONNECTS 80 86 90 6 2
CONNECT 39 81 79 33
CONNECT 40 82 80 34
CONNECT 39 81 83 45
CONNECT 40 82 84 46
C
C FWD SPAR, SPAR CAP, +45 TO -45.
C
LAMINATE DATABASE LAM.ARC
MATERIAL COMPOSITE 19,2

```
QUADRILATERAL  PLATE  TYPE 1 3
GENERATE CONNECTS 45 57 58 6 1
GENERATE CONNECTS 21 33 34 6 1
LAMINATE  DATABASE  LAM.ARC
MATERIAL  COMPOSITE 11,2
QUADRILATERAL  PLATE  TYPE 1 3
CONNECT 45 83 84 46
CONNECT 33 79 80 34
CONNECT 79 85 86 80
CONNECT 83 89 90 84
C
C FWD SPAR, SPAR CAP, (+45 TO +90) AND (-45 TO -90).
C
LAMINATE  DATABASE  LAM.ARC
MATERIAL  COMPOSITE 19,2
QUADRILATERAL  PLATE  TYPE 1 3
GENERATE CONNECTS 57 75 76 6 1
GENERATE CONNECTS 3 21 22 6 1
C
C FWD SPAR, INNER SPAR CAP, +90 TO -90.
C
LAMINATE  DATABASE  LAM.ARC
MATERIAL  COMPOSITE 12,2
QUADRILATERAL  PLATE  TYPE 1 3
GENERATE CONNECTS 2 74 77 6 3
C
C REAR SPAR, SHEAR WEB, (+45 TO +90) AND (-45 TO -90).
C
LAMINATE  DATABASE  LAM.ARC
MATERIAL  COMPOSITE 18,2
QUADRILATERAL  PLATE  TYPE 1 3
GENERATE CONNECTS 102 114 115 4 1
GENERATE CONNECTS 101 113 116 4 3
GENERATE CONNECTS 138 150 151 4 1
GENERATE CONNECTS 137 149 152 4 3
C
C REAR SPAR, SHEAR WEB, +45 TO -45.
C
LAMINATE  DATABASE  LAM.ARC
MATERIAL  COMPOSITE 18,2
QUADRILATERIAL  PLATE  TYPE 1 3
GENERATE CONNECTS 130 138 139 4 1
GENERATE CONNECTS 114 122 123 4 1
```

```
GENERATE CONNECTS 129 137 140 4 3
GENERATE CONNECTS 113 121 124 4 3
GENERATE CONNECTS 122 123 131 1 4
GENERATE CONNECTS 121 124 132 3 4
GENERATE CONNECTS 153 159 163 6 2
GENERATE CONNECTS 154 160 164 6 2
CONNECT 128 156 154 124
CONNECT 127 155 157 131
CONNECT 127 155 153 123
CONNECT 128 156 158 132
C
C REAR SPAR, SPAR CAP, +45 TO -45.
C
LAMINATE  DATABASE  LAM.ARC
MATERIAL   COMPOSITE 15,2
QUADRILATERAL  PLATE  TYPE 1 3
GENERATE CONNECTS 115 123 124 4 1
GENERATE CONNECTS 131 139 140 4 1
GENERATE CONNECTS 113 137 138 4 1
CONNECT 153 159 160 154
CONNECT 157 163 164 158
CONNECT 123 153 154 124
CONNECT 131 157 158 132
C
C REAR SPAR, SPAR CAP, (+45 TO +90) AND (-45 TO -90).
C
LAMINATE  DATABASE  LAM.ARC
MATERIAL  COMPOSITE 19,2
QUADRILATERAL  PLATE  TYPE 1 3
GENERATE CONNECTS 101 113 114 4 1
GENERATE CONNECTS 103 115 116 4 1
GENERATE CONNECTS 137 149 150 4 1
GENERATE CONNECTS 135 151 152 4 1
C
C RIGID WING STRUCTURE DESIGNED TO EXHIBIT MINIMAL
C DEFORMATION WITHIN THE COMPONENT.
C
LAMINATE  DATABASE  LAM.ARC
MATERIAL  COMPOSITE 1,2
QUADRILATERAL  PLATE  TYPE 1 3
CONNECT 89 311 313 90
CONNECT 85 312 314 86
CONNECT 89 311 312 85
```

```
CONNECT 90 313 314 86
CONNECT 163 317 318 159
CONNECT 164 315 316 160
CONNECT 163 164 315 317
CONNECT 159 160 316 318
CONNECT 163 307 319 317
CONNECT 159 308 320 318
CONNECT 90 164 315 313
CONNECT 86 160 316 314
GENERATE CONNECT 307 308 320 1 12
GENERATE CONNECT 301 302 310 1 8
CONNECT 301 89 311 309
CONNECT 302 85 312 310
CONNECT 301 302 85 89
CONNECT 85 86 90 89
CONNECT 86 90 163 159
CONNECT 163 159 160 164
CONNECT 160 164 307 308
GENERATE CONNECT 309 310 320 1 2
END
```

B. MSC/PAL2 LOAD FILE

```
DISPLACEMENTS  APPLIED 21
ALL 0 1 73 74 72 1
ALL 0 5 77 78 72 1
ALL 0 101 149 150 48 1
DISPLACEMENTS  APPLIED 1
ALL 0 103 104 151 152
ALL 0 3 4 75 76
FORCES AND MOMENTS APPLIED 0
FY 314 480
SOLVE
QUIT
```

C. MATLAB® PLY ANGLE OPTIMIZATION PROGRAM

```
% ABD MATRIX OPTIMIZATION
% 1.) Enter physical properties EE11 through G12.
% 2.) Select the desired QBxx values to be summed
%       by QBTOT.
% 3.) Enter the correct ylabel value.
EE11=1.97E7;
EE22=1.2E6;
U12=2.549E-1;
U21=1.558E-2;
G12=9.368E5;
    Q11=EE11/(1-U12*U21);
    Q22=EE22/(1-U12*U21);
    Q12=U21*EE11/(1-U12*U21);
    Q66=G12;
b=linspace(0,90,91);
QBTOT=eye(1,91);
for Z=1:1:91,
B=b(Z)*3.1415927/180;
    QB11=Q11*(cos(B))^4+2*(Q12+2*Q66)*
            (sin(B)^2)*(cos(B))^2+Q22*(sin(B))^4;
    QB22=Q11*(sin(B))^4+2*(Q12+2*Q66)*
            (sin(B)^2)*(cos(B))^2+Q22*(cos(B))^4;
    QB12=(Q11+Q22-4*Q66)*(sin(B))^2*(cos(B))^2+
            Q12*((sin(B))^4+(cos(B))^4);
    QB66=(Q11+Q22-2*Q12-2*Q66)*(sin(B))^2*
            (cos(B))^2+Q66*((sin(B))^4+(cos(B))^4);
    QB16=(Q11-Q22-2*Q66)*sin(B)*(cos(B))^3+
            (Q12-Q22+2*Q66)*(sin(B))^3*cos(B);
    QB26=(Q11-Q22-2*Q66)*(sin(B))^3*cos(B)+
            (Q12-Q22+2*Q66)*sin(B)*(cos(B))^3;
QBTOT(Z)=QB11+QB12;
end

plot(b,QBTOT):xlabel('Ply angle, degrees'):ylabel('A11+A12'):grid
```

APPENDIX C

A. PLY PROPERTIES

	MATERIAL 1	MATERIAL 2	MATERIAL 3
E1	3.100E+05	7.568E+06	1.945E+07
E2	2.067E+05	1.994E+06	1.193E+06
G12	2.314E+05	8.433E+05	9.135E+05
U12	0.270E+00	0.259E+00	0.256E+00
ALPH1	2.220E-05	2.019E-06	8.564E-08
ALPH2	1.056E-05	1.288E-05	1.785E-05
ALPH12	0.000E+00	0.000E+00	0.000E+00
RHO	6.714E-02	7.100E-02	5.626E-02
FT1	0.000E+00	2.980E+05	2.500E+05
FT2	0.000E+00	1.500E+04	1.500E+04
FC1	0.000E+00	-1.180E+05	-1.600E+05
FC2	0.000E+00	-3.000E+04	-3.000E+04
F12	0.000E+00	9.000E+03	1.400E+04
FAW	1.085E-04	3.300E-02	6.600E-02
RC	3.000E-01	2.648E-01	3.175E-01
VV	7.143E-02	2.000E-02	2.000E-02
TPLY	2.309E-03	6.322E-01	1.719E+00
G13	0.000E+00	0.000E+00	0.000E+00
G23	0.000E+00	0.000E+00	0.000E+00
F13	0.000E+00	0.000E+00	0.000E+00

B. LAMINATE LAYUP

1. Laminate layup location 'A'

LYR	MAT	THICK	ANGLE	ID
1	1	0.00225	45.0	12
2	1	0.00225	-45.0	11
3	1	0.00225	45.0	10
4	1	0.00225	-45.0	9
5	1	0.00225	45.0	8
6	1	0.00225	-45.0	7
7	1	0.00225	-45.0	6
8	1	0.00225	45.0	5
9	1	0.00225	-45.0	4
10	1	0.00225	45.0	3
11	1	0.00225	-45.0	2
12	1	0.00225	45.0	1

2. Laminate layup location 'B' and 'D'

LYR	MAT	THICK	ANGLE	ID
1	1	0.0022	45.0	16
2	1	0.0022	-45.0	15
3	1	0.0022	45.0	14
4	1	0.0022	-45.0	13
5	1	0.0022	45.0	12
6	1	0.0022	-45.0	11
7	1	0.0022	45.0	10
8	1	0.0022	-45.0	9
9	1	0.0022	-45.0	8
10	1	0.0022	45.0	7
11	1	0.0022	-45.0	6
12	1	0.0022	45.0	5
13	1	0.0022	-45.0	4
14	1	0.0022	45.0	3
15	1	0.0022	-45.0	2
16	1	0.0022	45.0	1

3. Laminate layup location 'C'

LYR	MAT	THICK	ANGLE	ID
1	1	0.00225	45.0	20
2	1	0.00225	-45.0	19
3	1	0.00225	45.0	18
4	1	0.00225	-45.0	17
5	1	0.00225	45.0	16
6	1	0.00225	-45.0	15
7	1	0.00225	45.0	14
8	1	0.00225	-45.0	13
9	1	0.00225	45.0	12
10	1	0.00225	-45.0	11
11	1	0.00225	-45.0	10
12	1	0.00225	45.0	9
13	1	0.00225	-45.0	8
14	1	0.00225	45.0	7
15	1	0.00225	-45.0	6
16	1	0.00225	45.0	5
17	1	0.00225	-45.0	4
18	1	0.00225	45.0	3
19	1	0.00225	-45.0	2
20	1	0.00225	45.0	1

4. Laminate layup location 'AA' AND 'EE'

LYR	MAT	THICK	ANGLE	ID
1	2	0.0070	0.0	6
2	2	0.0070	0.0	5
3	2	0.0070	0.0	4
4	2	0.0070	0.0	3
5	3	0.0120	0.0	2
6	3	0.0120	0.0	1

5. Laminate layup location 'BB'

LYR	MAT	THICK	ANGLE	ID
1	2	0.0070	0.0	11
2	2	0.0070	0.0	10
3	2	0.0070	0.0	9
4	2	0.0070	0.0	8
5	2	0.0070	0.0	7
6	2	0.0070	0.0	6
7	2	0.0070	0.0	5
8	2	0.0070	0.0	4
9	3	0.0120	0.0	3
10	3	0.0120	0.0	2
11	3	0.0120	0.0	1

6. Laminate layup location 'CC'

LYR	MAT	THICK	ANGLE	ID
1	2	0.0070	0.0	3
2	2	0.0070	0.0	2
3	2	0.0070	0.0	1

7. Laminate layup location 'DD'

LYR	MAT	THICK	ANGLE	ID
1	2	0.0070	0.0	4
2	2	0.0070	0.0	3
3	2	0.0070	0.0	2
4	3	0.0120	0.0	1

C. LAMINATE PROPERTIES

1. Laminate 'A' properties

A

1.070E+04	-1.789E+03	-2.569E-06
-1.789E+03	1.070E+04	-5.359E-09
-2.569E-06	-5.359E-09	2.874E+03

B

-2.214E-05	3.187E-06	-2.814E-08
3.187E-06	-2.214E-05	3.362E-08
-2.814E-08	3.362E-08	-4.524E-06

S

0.000E+00	0.000E+00
0.000E+00	0.000E+00

D

6.503E-01	-1.087E-01	1.113E-02
-1.087E-01	6.503E-01	1.113E-02
1.113E-02	1.113E-02	1.746E-01

A-PRIME

9.611E-05	1.606E-05	8.593E-14
1.606E-05	9.611E-05	1.454E-14
8.593E-14	1.454E-14	3.480E-04

B-PRIME

3.303E-09	6.320E-10	-2.386E-10
6.326E-10	3.304E-09	-2.669E-10
-1.735E-10	-2.018E-10	9.041E-09

S-PRIME

0.000E+00	0.000E+00
0.000E+00	0.000E+00

D-PRIME

1.584E+00	2.668E-01	-1.181E-01
2.668E-01	1.584E+00	-1.181E-01
-1.181E-01	-1.181E-01	5.743E+00

THERMAL COEFFICIENTS OF FORCE   1.546E-01   1.546E-01   -2.509E-10
                      MOMENT   -2.920E-10   -3.344E-10   1.280E-12

ALPHAX= 1.734E-05   ALPHAY= 1.734E-05   ALPHAXY=-7.401E-14
ALPHMX= 5.620E-11   ALPHMY= 5.396E-13   ALPHMXY= 5.449E-11

EX= 3.854E+05   EY= 3.854E+05   GXY= 1.064E+05   UXY=-.167   RHO= 1.813E-03
TTH= 0.02700   ZBAR= 0.01350

2. Laminate 'B' and 'D' properties

A

1.427E+04	-2.385E+03	-1.153E-06
-2.385E+03	1.427E+04	1.410E-06
-1.153E-06	1.410E-06	3.832E+03

B

9.711E-06	-5.148E-05	-1.459E-06
-5.148E-05	9.711E-06	-1.359E-06
-1.359E-06	-1.459E-06	-1.117E-05

S

0.000E+00	0.000E+00
0.000E+00	0.000E+00

D

1.541E+00	-2.576E-01	1.979E-02
-2.576E-01	1.541E+00	1.979E-02
1.979E-02	1.979E-02	4.138E-01

A-PRIME

7.208E-05	1.205E-05	1.726E-14
1.205E-05	7.208E-05	-2.290E-14
1.726E-14	-2.290E-14	2.610E-04

B-PRIME

2.387E-09	3.451E-10	1.630E-10
3.453E-10	2.387E-09	1.484E-10
1.854E-10	1.708E-10	7.027E-09

S-PRIME

0.000E+00	0.000E+00
0.000E+00	0.000E+00

D-PRIME

6.680E-01	1.121E-01	-3.731E-02
1.121E-01	6.680E-01	-3.731E-02
-3.731E-02	-3.731E-02	2.420E+00

THERMAL COEFFICIENTS OF FORCE 2.061E-01 2.061E-01 9.519E-11
                        MOMENT -7.380E-10 -7.997E-10 -1.084E-10

ALPHAX= 1.734E-05   ALPHAY= 1.734E-05   ALPHAXY= 2.840E-14
ALPHMX=-1.549E-11   ALPHMY=-4.973E-11   ALPHMXY=-1.666E-10

EX= 3.854E+05   EY= 3.854E+05   GXY= 1.064E+05   UXY=-.167   RHO= 2.417E-03
TTH= 0.03600   ZBAR=0.01800

3. Laminate 'C' properties

A

1.784E+04	-2.982E+03	-1.698E-07
-2.982E+03	1.784E+04	2.394E-06
-1.698E-07	2.394E-06	4.790E+03

B

8.796E-06	-6.249E-05	-1.232E-06
-6.249E-05	8.796E-06	-1.152E-06
-1.232E-06	-1.152E-06	-1.085E-05

S

0.000E+00	0.000E+00
0.000E+00	0.000E+00

D

3.011E+00	-5.031E-01	3.093E-02
-5.031E-01	3.011E+00	3.093E-02
3.093E-02	3.093E-02	8.083E-01

A-PRIME

9.637E-06	5.766E-05	-2.771E-15
5.766E-05	9.637E-06	-2.847E-14
-2.771E-15	-2.847E-14	2.088E-04

B-PRIME

2.329E-10	1.207E-09	4.650E-11
1.207E-09	2.329E-10	4.177E-11
6.711E-11	6.238E-11	2.796E-09

S-PRIME

0.000E+00	0.000E+00
0.000E+00	0.000E+00

D-PRIME

3.419E-01	5.730E-02	-1.527E-02
5.730E-02	3.419E-01	-1.527E-02
-1.527E-02	-1.527E-02	1.238E+00

THERMAL COEFFICIENTS OF FORCE   2.576E-01   2.576E-01   -1.312E-10
MOMENT   -8.673E-10   -8.029E-10   -7.498E-11

ALPHAX= 1.734E-05   ALPHAY= 1.734E-05   ALPHAXY=-2.811E-14
ALPHMX= 2.961E-11   ALPHMY= 4.796E-11   ALPHMXY=-5.005E-11

EX= 3.854E+05   EY= 3.854E+05   GXY= 1.064E+05   UXY=-.167   RHO= 3.021E-03
TTH= 0.04500   ZBAR= 0.02250

4. Laminate 'AA' and 'EE' properties

A

6.844E+05	2.207E+04	0.000E+00
2.207E+04	8.558E+04	0.000E+00
0.000E+00	0.000E+00	4.554E+04

B

3.972E+03	-7.346E+01	0.000E+00
-7.346E+01	-2.795E+02	0.000E+00
0.000E+00	0.000E+00	2.359E+01

S

0.000E+00	0.000E+00
0.000E+00	0.000E+00

D

1.595E+02	4.874E+00	0.000E+00
4.874E+00	1.891E+01	0.000E+00
0.000E+00	0.000E+00	1.029E+01

A-PRIME

1.730E-06	-4.465E-07	0.000E+00
-4.465E-07	1.239E-05	0.000E+00
0.000E+00	0.000E+00	2.199E-05

B-PRIME

-4.364E-05	1.137E-05	0.000E+00
1.137E-05	1.785E-04	0.000E+00
0.000E+00	0.000E+00	-5.039E-05

S-PRIME

0.000E+00	0.000E+00
0.000E+00	0.000E+00

D-PRIME

7.420E-03	-1.914E-03	0.000E+00
-1.914E-03	5.606E-02	0.000E+00
0.000E+00	0.000E+00	9.727E-02

THERMAL COEFFICIENTS OF FORCE   7.965E-01   1.275E+00   0.000E+00

MOMENT -5.098E-03 -1.944E-03   0.000E+00

ALPHAX= 1.009E-06   ALPHAY= 1.504E-05   ALPHAXY= 0.000E+00
ALPHMX=-5.436E-05   ALPHMY= 1.375E-04   ALPHMXY= 0.000E+00

EX= 1.112E+07   EY= 1.552E+06   GXY= 8.747E+05   UXY=0.258   RHO= 3.338E-03
TTH= 0.05200   ZBAR= 0.02600

5. Laminate 'BB' properties

A

1.134E+06	4.045E+04	0.000E+00
4.045E+04	1.568E+05	0.000E+00
0.000E+00	0.000E+00	8.011E+04

B

1.192E+04	-2.204E+02	0.000E+00
-2.204E+02	-8.385E+02	0.000E+00
0.000E+00	0.000E+00	7.077E+01

S

0.000E+00	0.000E+00
0.000E+00	0.000E+00

D

8.796E+02	2.706E+01	0.000E+00
2.706E+01	1.050E+02	0.000E+00
0.000E+00	0.000E+00	5.698E+01

A-PRIME

1.042E-06	-2.691E-07	0.000E+00
-2.691E-07	6.733E-06	0.000E+00
0.000E+00	0.000E+00	1.250E-05

B-PRIME

-1.430E-05	3.725E-06	0.000E+00
3.725E-06	5.224E-05	0.000E+00
0.000E+00	0.000E+00	-1.552E-05

S-PRIME

0.000E+00	0.000E+00
0.000E+00	0.000E+00

D-PRIME

1.342E-03	-3.463E-04	0.000E+00
-3.463E-04	1.004E-02	0.000E+00
0.000E+00	0.000E+00	1.757E-02

THERMAL COEFFICIENTS OF FORCE   1.507E+00   2.294E+00   0.000E+00
MOMENT   -1.529E-02   -5.831E-03   0.000E+00

ALPHAX= 1.150E-06   ALPHAY= 1.468E-05   ALPHAXY= 0.000E+00
ALPHMX=-3.152E-05   ALPHMY= 7.221E-05   ALPHMXY= 0.000E+00

EX= 1.043E+07   EY= 1.614E+06   GXY= 8.698E+05   UXY=0.258   RHO= 6.001E-03
TTI1= 0.09200   ZBAR= 0.04600

6. Laminate 'CC' properties

```
            A                              B
1.618E+05  1.103E+04  0.000E+00    -9.917E-05  -6.157E-06   0.000E+00
1.103E+04  4.262E+04  0.000E+00    -6.157E-06  -2.351E-05   0.000E+00
0.000E+00  0.000E+00  1.771E+04     0.000E+00   0.000E+00  -1.083E-05

            S                              D
0.000E+00  0.000E+00               5.946E+00   4.054E-01   0.000E+00
0.000E+00  0.000E+00               4.054E-01   1.566E+00   0.000E+00
                                   0.000E+00   0.000E+00   6.508E-01

         A-PRIME                         B-PRIME
 6.292E-06  -1.628E-06  0.000E+00   1.051E-10  -2.691E-11   0.000E+00
-1.628E-06   2.388E-05  0.000E+00  -2.691E-11   3.591E-10   0.000E+00
 0.000E+00   0.000E+00  5.647E-05   0.000E+00   0.000E+00   9.396E-10

         S-PRIME                         D-PRIME
0.000E+00  0.000E+00                1.712E-01  -4.431E-02   0.000E+00
0.000E+00  0.000E+00               -4.431E-02   6.499E-01   0.000E+00
                                    0.000E+00   0.000E+00   1.536E+00


THERMAL COEFFICIENTS OF FORCE    4.687E-01   5.711E-01   0.000E+00
                        MOMENT   -2.665E-10  -3.108E-10   0.000E+00


ALPHAX= 2.019E-06    ALPHAY= 1.288E-05    ALPHAXY= 0.000E+00
ALPHMX= 2.031E-12    ALPHMY= 2.316E-12    ALPHMXY= 0.000E+00

EX= 7.568E+06    EY= 1.994E+06    GXY= 8.433E+05    UXY=0.259    RHO= 1.491E-03
TTH= 0.02100     ZBAR= 0.01050
```

7. Laminate 'DD' properties

```
            A                                      B
3.961E+05   1.471E+04   0.000E+00       1.490E+03   -2.755E+01   0.000E+00
1.471E+04   5.700E+04   0.000E+00      -2.755E+01   -1.048E+02   0.000E+00
0.000E+00   0.000E+00   2.867E+04       0.000E+00    0.000E+00   8.847E+00

            S                                      D
0.000E+00   0.000E+00                   4.042E+01    1.252E+00   0.000E+00
0.000E+00   0.000E+00                   1.252E+00    4.858E+00   0.000E+00
                                        0.000E+00    0.000E+00   2.629E+00

         A-PRIME                                B-PRIME
2.972E-06   -7.676E-07   0.000E+00     -1.110E-04    2.890E-05   0.000E+00
-7.676E-07   1.847E-05   0.000E+00      2.890E-05    3.867E-04   0.000E+00
0.000E+00    0.000E+00   3.491E-05      0.000E+00    0.000E+00  -1.175E-04

         S-PRIME                                D-PRIME
0.000E+00   0.000E+00                   2.909E-02   -7.504E-03   0.000E+00
0.000E+00   0.000E+00                  -7.504E-03    2.163E-01   0.000E+00
                                        0.000E+00    0.000E+00   3.808E-01
```

THERMAL COEFFICIENTS OF FORCE   5.545E-01   8.280E-01   0.000E+00
                       MOMENT   -1.912E-03 -7.289E-04   0.000E+00

ALPHAX= 1.204E-06   ALPHAY= 1.453E-05   ALPHAXY= 0.000E+00
ALPHMX=-8.773E-05   ALPHMY= 1.929E-04   ALPHMXY= 0.000E+00

EX= 1.019E+07   EY= 1.641E+06   GXY= 8.680E+05   UXY=0.258   RHO= 2.166E-03
TTH= 0.03300 ZBAR= 0.01650

APPENDIX D

A. TEST STAND CALCULATIONS

Static analysis was performed on the components listed in Table D1.

Table D1. COMPONENT ANALYSIS.

Component	Analysis
Bearings	Static load.
Shaft	Bending, shear, torsion.
Extension	Bending, shear, torsion.
Bracket	Bending, shear torsion.

The force on each load-carrying member was calculated from the weight of the components and the forces applied during engine runs. A vector representing the weight of each component was place at its center of gravity as shown in Figure D1. The engine loads were calculated for a 29 Hp motor producing 150 lbs of static thrust.

A strengths of materials approach was performed using the equations D1 through D8 [Ref. 15].

static load: $\sum F = 0$ (eq. D1)

$\sum M = 0$ (eq. D2)

shear: $\tau_{max} = k \dfrac{V}{A}$, solid beam   (eq. D3)

$\tau_{max} = \dfrac{VQ}{It}$, at neutral axis   (eq. D4)

bending: $\sigma_{max} = \dfrac{Mc}{I}$ (eq. D5)

torque: $\tau_{max} = \dfrac{T\,c}{J}$,circular shaft   (eq. D6)

$\tau_{max} = \dfrac{T}{2\,t\,\alpha}$,square beam   (eq. D7)

normal force: $\sigma = \dfrac{P}{A}$ (eq. D8)

The maximum stress components were calculated for each member and applied to Von Mises' yield criterion (eq. D9) to compare to the material yield values.

$$\frac{1}{6}\left[\left(\sigma_{xx} - \sigma_{yy}\right)^2 + \left(\sigma_{yy} - \sigma_{zz}\right)^2 + \left(\sigma_{xx} - \sigma_{zz}\right)^2 + 6\sigma_{yz} + 6\sigma_{xz} + 6\sigma_{xy}\right] < \frac{Y^2}{3} \qquad \text{(eq. D9)}$$
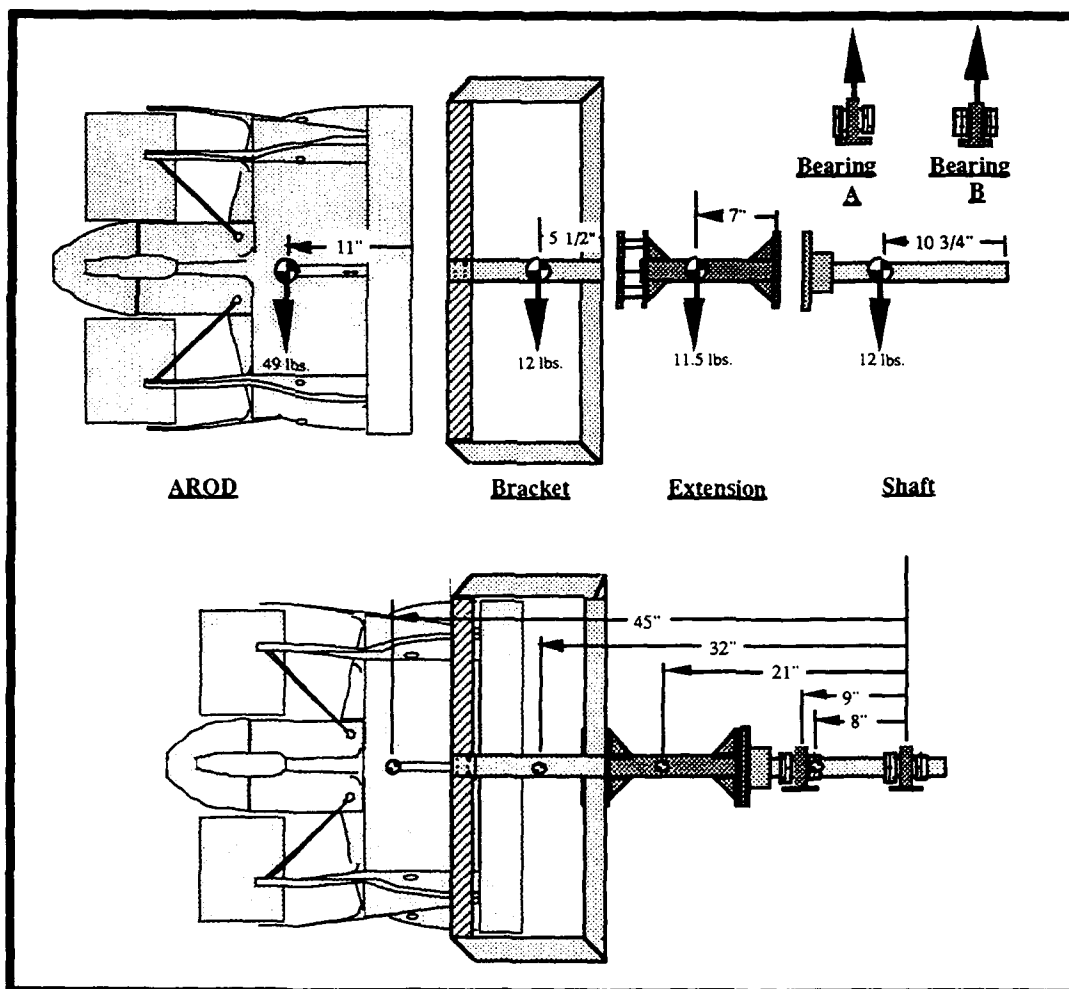
Figure D1. Test stand components.

A load applied to the engine produces an engine torque which creates torsion on the axial members of the test stand. Torque produce by the engine is a function of RPM and horsepower as related in equation D10. The AROD uses a Herbranson engine rated at 29 Hp at 8000 RPM.

$$\text{Torque}_{(\text{in.} \cdot \text{lbs.})} = \frac{\text{Hp}}{2\,\pi\,\text{RPM}} \bullet \left(\frac{550\ \frac{\text{ft.} \cdot \text{lbs.}}{\text{sec.}}}{1\ \text{Hp}} \right) \bullet \left(60\,\tfrac{\text{sec.}}{\text{min.}} \right) \bullet \left(12\,\tfrac{\text{in.}}{\text{ft.}} \right) \qquad \text{(eq. D10)}$$

B. BEARINGS

The bearings used were a Thompson PB-24 and a Thompson Super24 linear bearing. Description of these two bearings are listed is Table D2 [Ref. 15, p.19]. The bearings are mounted in self-aligning pillow blocks 9 inches apart. The sum of the forces in the vertical direction was calculated using equation D1 to determine the static load on each bearing.

Table D2. BEARING CHARACTERISTICS.

Bore diameter, inches	Bearing diameter, inches	Length, inches	Normal load rating, lbs.	Maximum load rating, lbs.
1.5	2.375	3.0	1560	2000

$$\sum F_{vertical} = 0 \qquad\qquad\qquad\qquad \text{(eq. D1)}$$

$$F_{Bearing\,A} + F_{Bearing\,B} + F_{AROD} + F_{Bracket} + F_{Extension} + F_{Shaft} = 0$$

$$F_{Bearing\,A} + F_{Bearing\,B} - 49_{\,lbs.} - 12_{\,lbs.} - 11.5_{\,lbs.} - 12_{\,lbs.} = 0$$

$$F_{Bearing\,A} + F_{Bearing\,B} = 84.5 \text{ lbs.}$$

$$\sum M_{Bearing\,B} = 0 \qquad\qquad\qquad\qquad \text{(eq. D2)}$$

$$F_{Bearing\,A}d_{Bearing\,A} + F_{AROD}d_{AROD} + F_{Bracket}d_{Bracket} + F_{Extension}d_{Extension}$$

$$+ F_{Shaft}d_{Shaft} = 0$$

$$F_{Bearing\,A}(9_{\,in.}) + 49_{\,lbs.}(45_{\,in.}) + 12_{\,lbs.}(32_{\,in.}) + 11.5_{\,lbs.}(21_{\,in.})$$

$$+ 12_{\,lbs.}(8_{\,in.}) = 0$$

$$F_{Bearing\,A} = 314.5 \text{ lbs.} \qquad\qquad \text{(eq. D11)}$$

The value obtained from the sum of the moments was substituted into the equation representing the sum of the forces:

$$F_{Bearing\,A} + F_{Bearing\,B} = 84.5 \text{ lbs.}$$

$$F_{Bearing\,A} = 314.5 \text{ lbs.} \qquad\qquad \text{(eq. D11)}$$

$$F_{Bearing\,B} = 230 \text{ lbs.} \qquad\qquad \text{(eq. D12)}$$

The maximum static load from Table D2 was compared with the calculated static loads, (eq. D11) and (eq. D12), for each bearing. As shown, both bearings provide an ample load margin under the maximum rated value.

C. SHAFT

The shaft is constructed from hardened, highly polished steel described in Table D3. All forces generated on the test stand act on the shaft. Two groups of forces are present while the AROD is mounted on the test stand. When tests are not being performed, the weight of the AROD, bracket and extension apply a shear and bending load on the shaft. During engine tests an additional normal force due to thrust and torque due to horsepower are applied.

Table D3. SHAFT MATERIAL PROPERTIES.

Material	Treatment	σ_U ,psi	σ_Y ,psi	Rockwell HN	Brinell HN
AISI 440C	Case hardened	285,000	275,000	C60	610

The maximum shear load in the shaft was determined by summing the vertical forces acting to the left of the shaft shown in Figure D1. Denoting V as the shear force (eq. D1) becomes:

$$\sum F_{vertical} = 0 \qquad \text{(eq. D1)}$$

$$F_{AROD} + F_{Bracket} + F_{Extension} + V_{Shaft} = 0$$

$$- 49 \, lbs. - 12 \, lbs. - 11.5 \, lbs. + V_{Shaft} = 0$$

$$V_{Shaft} = 72.5 \, lbs.$$

The weight of the shaft was neglected since its weight is supported by the bearings and not the shaft itself.

The maximum stress due to the vertical shear component was calculated using equation D3, where k = 4/3 for a circular shaft.

$$\tau_{max} = k \frac{V}{A} \qquad \text{(eq. D3)}$$

$$= \frac{4}{3} \left(\frac{72.5 \, lbs.}{\pi (0.75 \, in.)^2} \right)$$

$$\tau_{max} = 54.7 \, psi.$$

A bending moment applied to the shaft results from the vertical forces applied to a moment arm originating at the left of bearing A. For these forces equation D2 becomes:

$$\sum M_{Shaft} = 0 \qquad \text{(eq. D2}$$

$$F_{AROD} d_{AROD} + F_{Bracket} d_{Bracket} + F_{Extension} d_{Extension} + M_{Shaft} = 0$$

$$49(34.5) + 12(21.5) + 11.5(10.5) + M_{Shaft} = 0$$

$$M_{Shaft} = 2069.25 \, in \bullet lbs.$$

Since the shaft is symmetric the compressive and tensile stresses are of equal magnitude and opposite sign. The maximum value is computed using equation D5.

$$\sigma_{max} = \frac{M\,c}{I} \qquad\qquad \text{(eq. D5)}$$

$$= \frac{2069.25 \text{ in.•lbs.} \; • \; 0.75 \text{ in.}}{0.2485 \text{ in.}^4}$$

$$\sigma_{max} = 6245.1 \text{ psi}$$

where $I = \frac{1}{4}\pi r^4$ and c is the radius of the shaft.

The values for the engine were substituted into equation D10.

$$T_{shaft} = \frac{29_{Hp} • 550\frac{\text{ft.•lbs}}{\text{sec.}} • 60\frac{\text{sec}}{\text{min.}} • 12\frac{\text{in.}}{\text{ft.}}}{2\,\pi • 8000_{RPM}}$$

$$T_{shaft} = 228.5 \text{ in.•lbs.}$$

The shear stress due resulting from torsion was calculated using equation D6.

$$\tau_{max} = \frac{T\,c}{J} \qquad\qquad \text{(eq. D6)}$$

$$= \frac{(228.5 \text{ in.•lbs.})(0.75 \text{ in.})}{(0.4970 \text{ in.}^4)}$$

$$\tau_{max} = 344.8 \text{ psi.}$$

where J is the polar moment of inertia, $J = \frac{1}{2}\pi c^4$ and c is the radius.

The final force applied to the shaft is the normal force due to the static thrust of the ducted fan. For this calculation the maximum thrust output was estimated at 150 lbs. Substituting this value for P into equation D8 provides

$$\sigma = \frac{P}{A} \qquad\qquad \text{(eq. D8)}$$

$$= \frac{150 \text{ lbs.}}{\pi\,(0.75 \text{ in.})^2}$$

$$\sigma = 84.9 \text{ psi.}$$

The results of these maximum values of shear, bending, torque and normal force are depicted in Figure D2.

Torque and normal force are constant throughout the shaft; however, bending and shear vary around the circumference. Bending is maximum on the upper and lower surface of the shaft and zero on the middle surface, while vertical shear is zero on the upper and lower surface and maximum on the middle surface. Two elements taken from the surface show the effects of these combined stresses. The stress values were applied to Von Mises' yield criterion, (eq. D9), to compute the maximum stress seen by the shaft.
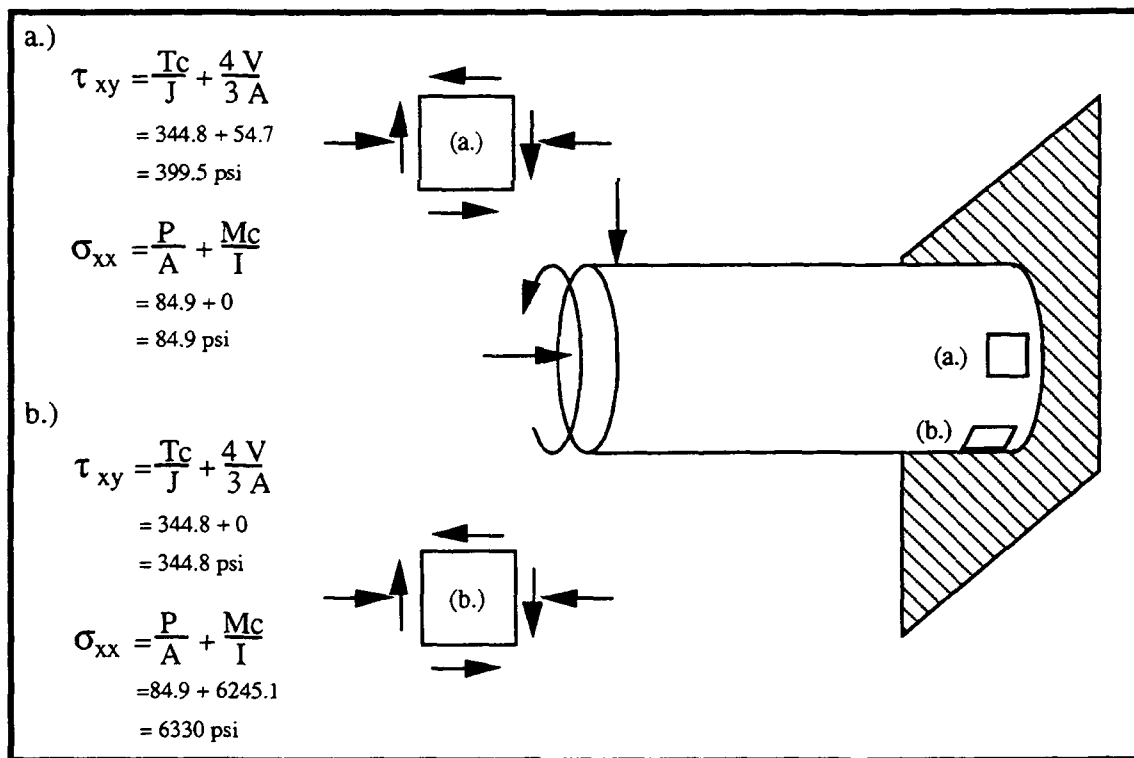

Figure D2. Stresses on the shaft.

$$\frac{1}{6}\left[\left(\sigma_{xx}-\sigma_{yy}\right)^2+\left(\sigma_{yy}-\sigma_{zz}\right)^2+\left(\sigma_{xx}-\sigma_{zz}\right)^2+6\sigma_{yz}+6\sigma_{xz}+6\sigma_{xy}\right]<\frac{Y^2}{3} \qquad \text{(eq. D9)}$$

$$\frac{1}{6}\left(\sigma_{xx}^2+\sigma_{xx}^2+6\sigma_{xy}^2\right)<\frac{Y^2}{3}$$

$$\sqrt{\sigma_{xx}^2+3\sigma_{xy}^2}<\sigma_{ys}$$

(a.) $\sqrt{84.9^2{}_{psi}+3(399.5{}_{psi})^2}<275,000{}_{psi}$ and (b.) $\sqrt{6330^2{}_{psi}+3(344.8{}_{psi})^2}<275,000{}_{psi}$

$697.1{}_{psi}<275,000{}_{psi}$ $\qquad\qquad\qquad$ $6358.1{}_{psi}<275,000{}_{psi}$

where Y is the yield strength from Table D2. Using Von Mises' yield criteria, the allowable load applied to the shaft produces stresses well below the yield point of the material.

D. EXTENSION

The extension was designed to locate the duct intake far enough away from the base of the stand to prevent any blockage of airflow. Since the extension was configured in a cantilever arrangement, it must support its own weight, that of the bracket and AROD, and any forces produced by the engine. The material selected for the extension was a low carbon steel, square tube. Its properties are listed in Table D4.

Table D4. EXTENSION MATERIAL PROPERTIES.

Material	Dimensions	Wall thickness	σ_{TU} ,psi	σ_{TY} ,psi	σ_{CU} ,psi	σ_{SY} ,psi
AISI 1025	2 in. x 2 in.	0.125 in.	55,000	36,000	36,000	35,000

The static analysis performed on the extension followed the same procedure as the analysis used for the shaft. The technique for calculating vertical shear and shear due to torsion varied slightly because of the different cross sectional area of the extension.

68

The vertical shear stress was calculated as

$$\sum F_{vertical} = 0 \qquad \text{(eq. D1)}$$

$$F_{AROD} + F_{Bracket} + F_{Extension} + V_{Extension} = 0$$

$$49_{lbs.} - 12_{lbs.} - 11.5_{lbs.} + V_{Extension} = 0$$

$$V_{Extension} = 72.5 \text{ lbs.}$$

$$\tau_{max} = \frac{VQ}{I t} \qquad \text{(eq. D4)}$$

$$= \frac{(72.5_{lbs.})(0.3301_{in.}{}^{3})}{(0.5518_{in.}{}^{4})(0.25_{in.})}$$

$$\tau_{max} = 173.5 \text{ psi.}$$

where $Q = A \bar{y}$ is the first moment of area and $I = \frac{1}{12}bh^3$ is the moment of inertia.

The maximum bending moment was calculated at the right end of the extension where the longest moment arm occurs. The maximum normal stress became

$$\sum M_{Extension} = 0 \qquad \text{(eq. D2)}$$

$$F_{AROD}d_{AROD} + F_{Bracket}d_{Bracket} + F_{Extension}d_{Extension} + M_{Extension} = 0$$

$$49_{lbs.}(31_{in.}) + 12_{lbs.}(18_{in.}) + 11.5_{lbs.}(7_{in.}) + M_{Extension} = 0$$

$$M_{Extension} = 1815.5 \text{ in.} \bullet \text{lbs.}$$

$$\sigma_{max} = \frac{M c}{I} \qquad \text{(eq. D5)}$$

$$= \frac{(1815.5_{in.\bullet lbs.})(1_{in.})}{(0.5518_{in.}{}^{4})}$$

$$\sigma_{max} = 3290 \text{ psi.}$$

where c is the distance from the neutral axis to the outer wall of the extension.

The engine torque and the thrust were identical to the values derived for the shaft. The shear and normal stress were calculated using equation D7 and D8.

$$\tau_{max} = \frac{T}{2\,t\,\alpha} \qquad\qquad\qquad \text{(eq. D7)}$$

$$= \frac{(228.5_{\,in.\,\bullet lbs.})}{2(0.125_{\,in.})(3.5156_{\,in.^2})}$$

$$\tau_{max} = 260 \text{ psi.}$$

$$\sigma_{max} = \frac{P}{A} \qquad\qquad\qquad \text{(eq. D8)}$$

$$= \frac{150_{\,lbs.}}{0.9375_{\,in.^4}}$$

$$\sigma_{max} = 160$$

where α is the area bound by the centerline of the tube walls and A is the cross sectional area of the square tube.

A combination of the stress values derived from maximum shear (a.) and maximum bending (b.) is shown in Figure D3.


a.)
$$\tau_{xy} = \frac{Tc}{J} + \frac{4\,V}{3\,A}$$
$$= 260 + 173.5$$
$$= 433.5 \text{ psi}$$

$$\sigma_{xx} = \frac{P}{A} + \frac{Mc}{I}$$
$$= 160 + 0$$
$$= 160 \text{ psi}$$

b.)
$$\tau_{xy} = \frac{Tc}{J} + \frac{4\,V}{3\,A}$$
$$= 260 + 0$$
$$= 260 \text{ psi}$$

$$\sigma_{xx} = \frac{P}{A} + \frac{Mc}{I}$$
$$= 160 + 3290$$
$$= 3450 \text{ psi}$$
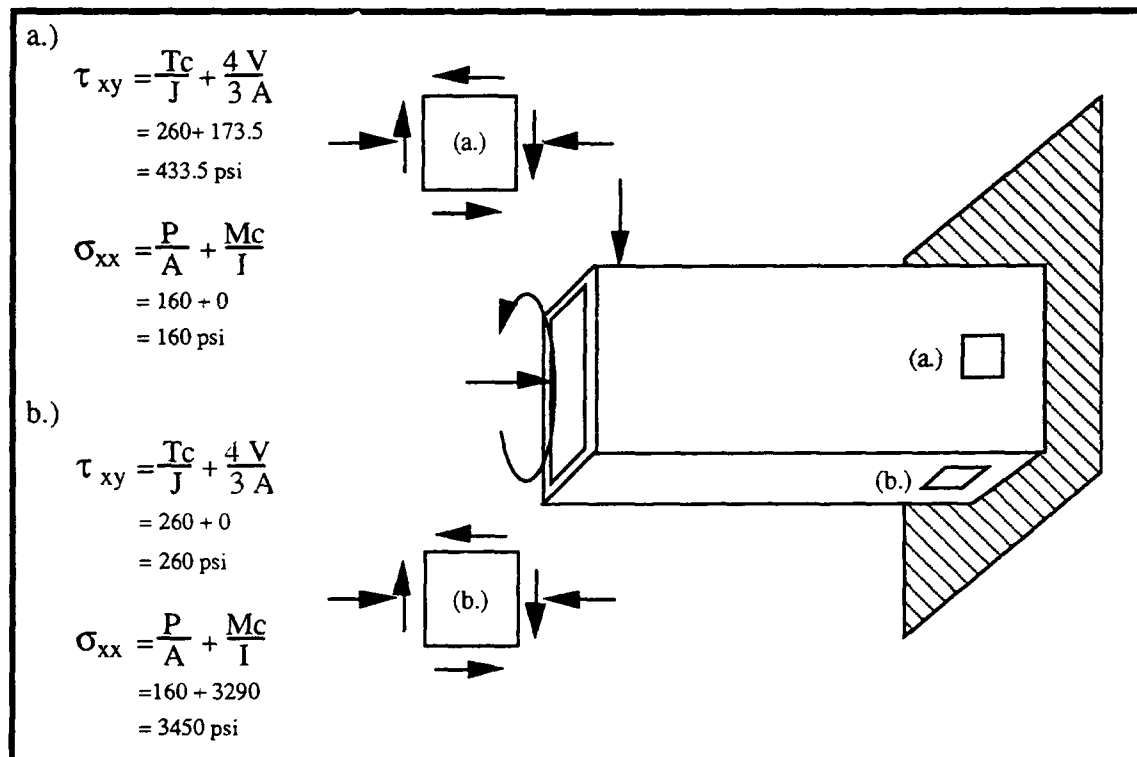
Figure D3. Stresses on the extension.

These values also were substituted into Von Mises' yield criterion.

$$\frac{1}{6}\left[\left(\sigma_{xx}-\sigma_{yy}\right)^2+\left(\sigma_{yy}-\sigma_{zz}\right)^2+\left(\sigma_{xx}-\sigma_{zz}\right)^2+6\sigma_{yz}+6\sigma_{xz}+6\sigma_{xy}\right]<\frac{Y^2}{3}\qquad\text{(eq. D9)}$$

$$\sqrt{\sigma_{xx}^2+3\sigma_{xy}^2}<\sigma_{ys}$$

(a.) $\sqrt{192^2{}_{psi}+3(433.5{}_{psi})^2}<36,000{}_{psi}$ and (b.) $\sqrt{3450^2{}_{psi}+3(260{}_{psi})^2}<36,000{}_{psi}$

$775{}_{psi}<36,000{}_{psi}$ $\qquad\qquad\qquad\qquad 3479.3{}_{psi}<36,000{}_{psi}$

E. BRACKET

Forces from the AROD are supported by the four arms of the bracket. The bracket was configured in an "X" to allow the fuel tank vents to be located at the highest possible elevation. Figure D4 shows a front and side view of the bracket configuration.
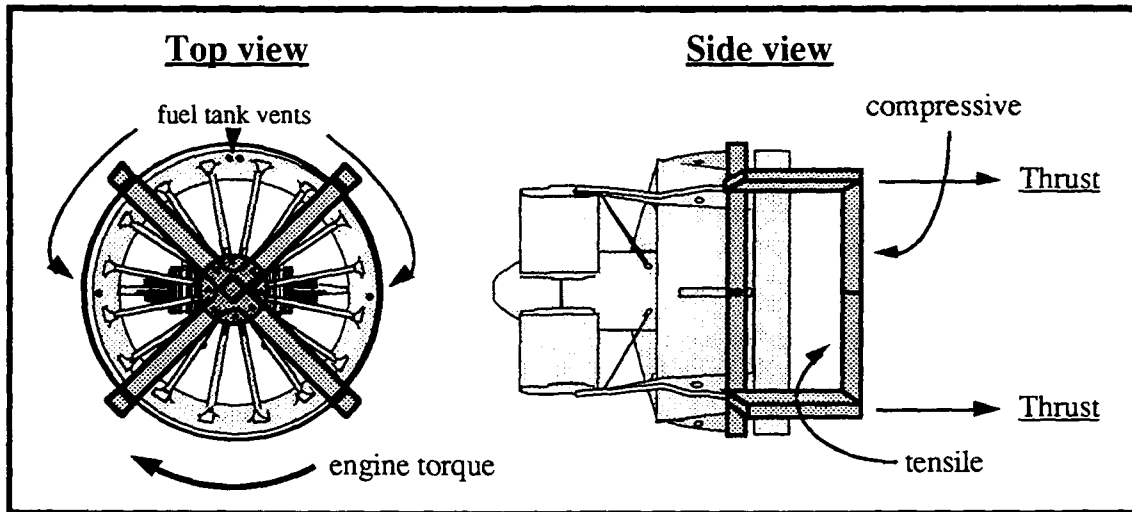

Figure D4. Bracket configuration.

The material used for the bracket was aluminum square tubing. The material properties are given in Table D5.

Table D5. BRACKET MATERIAL PROPERTIES.

Material	Dimensions	Wall thickness	σ_{TU} ,psi	σ_{TY} ,psi	σ_{CU} ,psi	σ_{SY} ,psi
6061-T6	2 in. x 2 in.	0.125 in.	42,000	37,000	42,000	20,000

Each arm of the bracket reacts differently to the forces of thrust, weight, and engine torque. The forces are additive in some locations and cancel one another in others. A diagram of normal and shear stress was drawn to identify which locations would undergo the maximum stress condition. Figure D5 illustrates the stress combination on the compressive and tensile side of the bracket.

Figure D5 identified the lower right arm of the bracket as experiencing the maximum combined stress condition. The values of normal and shear stress resulting from the forces on the bracket were calculated for the location immediately outboard from the extension flange were the greatest moment arm will occur. The resulting moment arm, 12 inches long, was used in the following calculations.

1. Engine torque

A rotational force is produced as the engine torque attempts to spin the bracket. This force produces a tangential shear in the rotational directional. A shearing stress (eq. D4) was obtained from the tangential shear.

$$V_{engine\ torque} = \frac{Torque}{distance} = \frac{228.5\ in.\cdot lbs.}{12\ in.} = 19\ lbs.\ ,\ total$$

$$V_{torque} = \frac{V_{engine\ torque}}{4} = 4.75\ lbs.\ ,\ per\ arm$$

$$\tau_{torque} = \frac{V\ Q}{I\ t} = \frac{(4.75\ lbs.)(0.3301\ in.^3)}{(0.5518\ in.^4)(0.25\ in.)} = 11.37\ psi.$$

Tensile

$+\sigma_{thrust} \; -\sigma_{F_1}$

$-\tau_{F_2} +\tau_{torque}$

$+\sigma_{thrust} \; -\sigma_{F_2}$

$-\tau_{torque} -\tau_{F_1}$

$-\tau_{torque} +\tau_{F_1}$

$+\sigma_{thrust} \; +\sigma_{F_2}$

$+\tau_{torque} +\tau_{F_2}$

$+\sigma_{thrust} \; +\sigma_{F_1}$

y   x

F_2 F_1

$F_1 = F_2 = Fcos(45°)$

$F = F_{AROD} + F_{Bracket}$

Compressive

$-\sigma_{thrust} +\sigma_{F_1}$

$+\tau_{F_2} -\tau_{torque}$

$-\sigma_{thrust} +\sigma_{F_2}$

$+\tau_{torque} +\tau_{F_1}$

$+\tau_{torque} -\tau_{F_1}$

$-\sigma_{thrust} -\sigma_{F_2}$

$-\tau_{torque} -\tau_{F_2}$
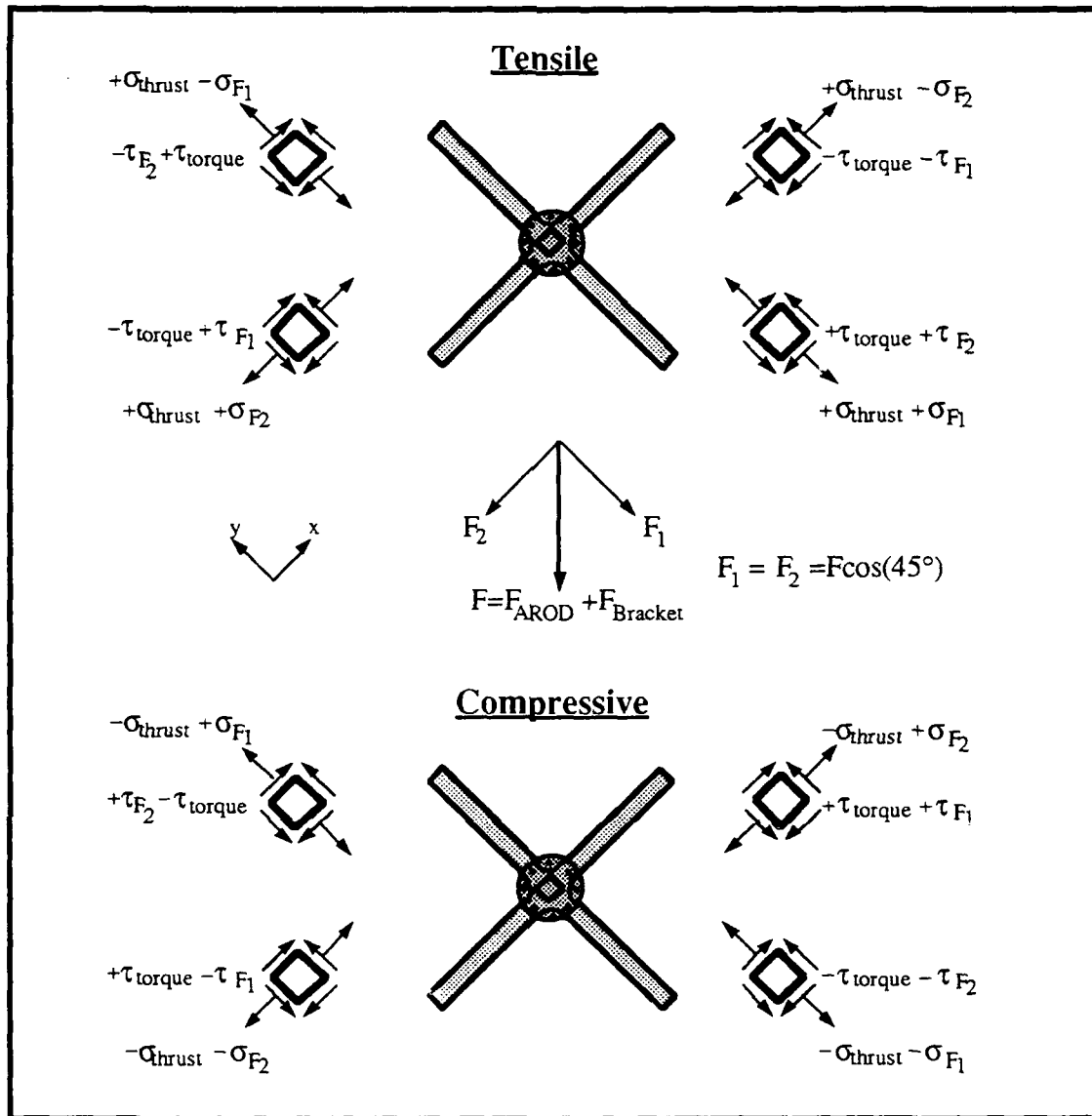
$-\sigma_{thrust} -\sigma_{F_1}$

Figure D5. Bracket stress components.

2. Engine thrust

A bending moment on the bracket arms results from static thrust applying a normal force at the outer duct diameter. A normal stress (eq. D5) was calculated from this bending moment.

73

$$M_{\text{total thrust}} = F_{\text{thrust}} + d_{\text{arm}} = 150 \text{ lbs.} \bullet 12 \text{ in.} = 1800 \text{ lb.} \bullet \text{in.} \quad , \text{ total}$$

$$M_{\text{thrust}} = \frac{M_{\text{total thrust}}}{4} = 450 \text{ i. } \bullet \text{ s.} \quad , \text{ per arm}$$

$$\sigma_{\text{thrust}} = \frac{M\,c}{I} = \frac{(450 \text{ in} \bullet \text{lbs.})(1 \text{ in.})}{0.5518 \text{ in.}^4} = 652.4 \text{ psi.}$$

3. Weight

The weight of the AROD and bracket were reduced to a single force located 13.34 inches from the centerline between the tensile and compressive faces of the bracket. The resultant 61-pound force was transformed into components perpendicular and parallel to the bracket arm. The component forces are shown as F_1 and F_2 in Figure D5.

$$F_{\text{total}} = F_{\text{AROD}} + F_{\text{Bracket}}$$
$$= 49 \text{ lbs.} + 12 \text{ lbs.}$$
$$F_{\text{total}} = 61 \text{ lbs.}$$
$$F = \frac{F_{\text{total}}}{4} = 15.24 \text{ lbs.}$$
$$F_1 = F_2 = F\cos(45°)$$
$$F_1 = F_2 = 10.78 \text{ lbs}$$

The F_2 component creates a shearing stress (eq. D7) by applying a twisting moment to the bracket arm.

$$T = F_2 x$$
$$= 10.78 \text{ lbs} \bullet 13.34 \text{ in}$$
$$T = 143.8 \text{ in} \bullet \text{lbs}$$
$$\tau = \frac{T}{2t\alpha}$$
$$= \frac{143.8 \text{ in} \bullet \text{lbs}}{2(.125 \text{ in})(3.5156 \text{ in}^2)}$$
$$\tau_{F_2} = 163.6 \text{ psi.}$$

74

The F_1 component creates a moment on the lower right bracket arm. This moment applies opposing stresses on the tensile and compressive faces of the bracket. The forces on each face was calculated through the summation of forces (eq. D1) and summation of moments (eq. D2).

$$\sum F_{vertical} = 0$$

$$F_{tens.} - F_{comp.} = -F_2$$

$$F_{tens.} - F_{comp.} = -10.78 \text{ lbs.}$$

$$\sum M_{resultant} = 0$$

$$F_{tens.} (12.34 \text{ in.}) - F_{comp.} (14.34 \text{ in.}) = 0$$

$$F_{tens.} = 1.1621 F_{comp.}$$

Solving these equations simultaneously and substituting the forces into equation D8 provided the normal stress. The σ_{F2} value was only calculated for the tensile face since the compressive normal stress will be less.

$$F_{comp.} = 66.5 \text{ lbs} \qquad \text{and} \qquad F_{tens.} = 77.28 \text{ lbs.}$$

$$\sigma_{F_2} = \frac{F_{tens.}}{A}$$

$$= \frac{77.28 \text{ lbs.}}{0.25 \text{ in.}}$$

$$\sigma_{F_2} = 309.2 \text{ psi.}$$

The shear and normal stress from the torque, thrust and weight components were added and applied to Von Mises' yield criterion.

$$\sigma_{xy} = \tau_{torque} + \tau_{F_2} = 11.37 \text{ psi} + 163.6 \text{ psi} = 174.94 \text{ psi}$$

$$\sigma_{xx} = \sigma_{thrust} + \sigma_{F_1} = 652.4 \text{ psi} + 309.2 \text{ psi} = 961.6 \text{ psi}$$

$$\frac{1}{6}\left[(\sigma_{xx} - \sigma_{yy})^2 + (\sigma_{yy} - \sigma_{zz})^2 + (\sigma_{xx} - \sigma_{zz})^2 + 6\sigma_{yz} + 6\sigma_{xz} + 6\sigma_{xy}\right] < \frac{Y^2}{3} \qquad \text{(eq. D9)}$$

$$\sqrt{\sigma_{xx}^2 + 3\sigma_{xy}^2} < \sigma_{ys}$$

$$\sqrt{961.6^2 \text{ ps.} + 3(174.94 \text{ psi})^2} < 37,000 \text{ psi}$$

$$1008.2 \text{ psi} < 37,000 \text{ psi}$$

REFERENCES

1. Wagner, William, *Lightning Bugs and Other Reconnaissance Drone,* Aero Publishers, Inc., 1982.

2. "Candidates for UAV Program Debut at Unmanned Aerial Vehicle Meeting." Aviation Week & Space Technology 26 August 1991: 50.

3. "Marines' Remotely Operated Device Will Use Aerial Fiber-Optic Link." Aviation Week & Space Technology 2 February 1987: 73.

4. Ellwood, Jeffrey L., *Design and Construction of a Composite Airframe for UAV Research.* Master's Thesis, Naval Postgraduate School, Monterey, California, June 1990.

5. Blanchette, Bryan M., *The Design and Construction of a Shiplaunched VTOL Unmanned Air Vehicle,* Master's Thesis, Naval Postgraduate School, Monterey, California, June 1990.

6. Brynestad, Mark A., *Investigation of the Flight Control Requirements of a Half-Scale Ducted Fan Unmanned Aerial Vehicle,* Master's Thesis, Naval Postgraduate School, Monterey, California, March 1992.

7. *Aquila Remotely Piloted Vehicle System Technology Demonstrator (RPV-STD) Program,* Lockheed Missiles & Space Company, Inc., by Alexander, Grover L., December 1977.

8. Black, Donald M., and Wainauski, Harry S., "Shrouded Propellers - A Comprehensive Study", AIAA Paper 68-994.

9. Raymer, Daniel P., *Aircraft Design: A Conceptual Approach,* American Institute of Aeronautics and Astronautics, 1989.

10. "MSC/pal2 Reference Manual", The MacNeal-Schwendler Corporation, Los Angeles, California, 1990.

11. *Moldless Composite Sandwich Homebuilt Aircraft Construction,* Rutan Aircraft Factory Inc., Mojave, California, 1983.

12. Jones, Robert M. *h.echanics of Composite Materials,* Hemisphere Publishing Corperation, 1975.

13. Niu, Michael C. Y., *Composite Airframe Structures,* Conmilit Press Ltd., 1992.

14. *Advanced Composite Fabrics,* Hexcel Trevarno Division, Dublin, California, 1983.

15. Beer, Ferdinand P., and Johnston, Russell E. Jr., *Mechanics of Materials,* McGraw-Hill, Inc., 1981.

INITIAL DISTRIBUTION LIST

		No. Copies
1.	Defense Technical Information Center Cameron Station Alexandria, Virginia 22304-6145	2
2.	Library, Code 52 Naval Postgraduate School Monterey, California 93943-5002	2
3.	Chairman Department of Aeronautics and Astronautics Code AA Naval Postgraduate School Monterey, California 93943-5000	1
4.	Commanding Officer Unmanned Aerial Vehicle Joint Project Office Naval Air Systems Command ATTN: PDA-14UD Washington, D.C. 20361-1014	1
5.	Mr. Rick J. Foch Naval Research Lab Code 5712 4555 Overlook Ave, S.W. Washington D.C. 20375	1
6.	Mr. Barth Shenk WL/FIMGD Wright-Patterson AFB, OH 45433	1
7.	Prof. Rick Howard Department of Aeronautics and Astronautics Code AA/Ho Naval Postgraduate School Monterey, California 93943-5000	3
8.	Prof. Conrad F. Newberry Department of Aeronautics and Astronautics Code AA/Ne Naval Postgraduate School Monterey, California 93943-5000	3

9. LT Gregory A. Kress 2
   1900 Parsonage Rd.
   Charleston, SC 29414